

1 **Determination of host cell proteins constituting the molecular microenvironment of**
2 **coronavirus replicase complexes by proximity-labeling**

3 V'kovski Philip^{1,2,3}, Gerber Markus^{1,2}, Kelly Jenna^{1,2,4}, Pfaender Stephanie^{1,2}, Ebert Nadine^{1,2},
4 Braga Lagache Sophie⁵, Simillion Cedric^{5,6}, Portmann Jasmine^{1,2}, Stalder Hanspeter^{1,2},
5 Gaschen Véronique⁷, Bruggmann Remy⁴, Stoffel Michael⁷, Heller Manfred⁵, Dijkman
6 Ronald^{1,2}, Thiel Volker^{1,2*}

7

8 ¹Institute of Virology and Immunology IVI, Bern, Switzerland, ²Department of Infectious
9 Diseases and Pathobiology, Vetsuisse Faculty, University of Bern, Bern, Switzerland,

10 ³Graduate School for Biomedical Science, University of Bern, Bern, Switzerland, ⁴Interfaculty

11 Bioinformatics Unit and SIB Swiss Institute of Bioinformatics, University of Bern,

12 Switzerland, ⁵Mass Spectrometry and Proteomics Core Facility, Department for BioMedical

13 Research (DBMR), University of Bern, Switzerland, ⁶Department of Clinical Research,

14 University of Bern, Switzerland, ⁷Division Veterinary Anatomy, Vetsuisse Faculty, University

15 of Bern, Bern, Switzerland.

16 *corresponding author: Volker Thiel, PhD, Department of Infectious Diseases and

17 Pathobiology, University of Bern, Länggassstrasse 122, 3012 Bern, Switzerland; Tel.: +41 31

18 631 2413; e-mail: Volker.thiel@vetsuisse.unibe.ch

19

20 **Keywords:** RNA virus, Coronavirus, replication complex, virus-host interaction, replication

21 compartments, proximity-labeling, viral replicase molecular microenvironment.

22 **Abstract**

23 Positive-sense RNA viruses hijack intracellular membranes that provide niches for viral RNA
24 synthesis and a platform for interactions with host proteins. However, little is known about host
25 factors at the interface between replicase complexes and the host cytoplasm. We engineered a
26 biotin ligase into a coronaviral replication/transcription complex (RTC) and identified >500
27 host proteins constituting the RTC microenvironment. siRNA-silencing of each RTC-proximal
28 host factor demonstrated importance of vesicular trafficking pathways, ubiquitin-dependent
29 and autophagy-related processes, and translation initiation factors. Notably, detection of
30 translation initiation factors at the RTC was instrumental to visualize and demonstrate active
31 translation proximal to replication complexes of several coronaviruses.

32 Collectively, we establish a spatial link between viral RNA synthesis and diverse host factors
33 of unprecedented breadth. Our data may serve as a paradigm for other positive-strand RNA
34 viruses and provide a starting point for a comprehensive analysis of critical virus-host
35 interactions that represent targets for therapeutic intervention.

36 **Introduction**

37 Positive-strand RNA viruses replicate at membranous structures that accommodate the viral
38 replication complex and facilitate RNA synthesis in the cytosol of infected host cells (1-5).
39 Rewiring host endomembranes is hypothesized to provide a privileged microenvironment
40 physically separated from the cytosol, thereby ensuring adequate concentrations of
41 macromolecules for viral RNA synthesis, preventing recognition of replication intermediates
42 such as double-stranded RNA (dsRNA) by cytosolic innate immune receptors (6, 7), and
43 providing a platform that facilitates molecular interactions with host cell proteins.

44 Ultrastructural studies have reported the origin, nature, and extent of membrane modifications
45 induced by coronaviruses (order *Nidovirales*, family *Coronaviridae*), which materialize as an
46 ER-derived network of interconnected double-membrane vesicles (DMVs) and convoluted
47 membranes (CM) in perinuclear regions of infected cells to which the viral
48 replication/transcription complex (RTC) is anchored (4, 8, 9). The RTC is generated by
49 translation of the genomic RNA into two large polyproteins that are extensively auto-
50 proteolytically processed by viral proteases to give rise to 16 processing end-products, termed
51 non-structural proteins (nsps) 1-16. Nsp1 is rapidly cleaved from the polyproteins and not
52 considered an integral component of the coronaviral RTC, but interferes with host cell
53 translation by inducing degradation of cellular mRNAs (10-12). Although it has not yet been
54 formally demonstrated, the remaining nsps (2-16) are thought to comprise the RTC and harbor
55 multiple enzymes and functions, such as de-ubiquitination, proteases, helicase, polymerase,
56 exo- and endonuclease, and N7- and 2'O-methyltransferases (13-18). Many of these functions
57 have been studied using reverse genetic approaches, which revealed their importance in virus-
58 host interactions (19-23). In most cases phenotypes were described via loss-of-function
59 mutagenesis, however, in the context of virus infection, the specific interactions of RTC
60 components with host cell factors remain largely unknown.

61 A number of individual host cell proteins have been shown to impact coronavirus replication
62 by using various screening methods, such as genome-wide siRNA, kinome, and yeast-two-
63 hybrid screens (24-28). Likewise, genome-wide CRISPR-based screens have been applied to
64 other positive-stranded RNA viruses, such as flaviviruses, and identified critical host proteins
65 required for replication (29, 30). Some of these proteins were described in the context of
66 distinct ER processes, such as N-linked glycosylation, ER-associated protein degradation
67 (ERAD), and signal peptide insertion and processing. Although individual proteins identified
68 by these screens may interact with viral replication complexes, they likely constitute only a
69 small fraction of the global replicase microenvironment.

70 To capture the full breadth of host cell proteins and cellular pathways that are spatially
71 associated with viral RTCs, we employed a proximity-based labeling approach involving a
72 promiscuous *E. coli*-derived biotin ligase (BirA_{R118G}). BirA_{R118G} biotinylates proximal (<10
73 nm) proteins in live cells without disrupting intracellular membranes or protein complexes, and
74 hence, does not rely on high affinity protein-protein interactions, but is able to permanently tag
75 transient interactions (31). Covalent protein biotinylation allows stringent lysis and washing
76 conditions during affinity purification and subsequent mass spectrometric identification of
77 captured factors. By engineering a recombinant MHV harboring BirA_{R118G} as an integral
78 component of the RTC we identified >500 host proteins reflecting the molecular
79 microenvironment of MHV replication structures. siRNA-mediated silencing of each of these
80 factors highlighted, amongst others, the functional importance of vesicular ER-Golgi apparatus
81 trafficking pathways, ubiquitin-dependent and autophagy-related catabolic processes, and
82 translation initiation factors. Importantly, the detection of active translation in close proximity
83 to the viral RTC highlighted the critical involvement of translation initiation factors during
84 coronavirus replication. Collectively, the determination of the coronavirus RTC-associated
85 microenvironment provides a functional and spatial link between conserved host cell processes

86 and viral RNA synthesis, and highlights potential targets for the development of novel antiviral
87 agents.

88

89 **Results**

90 **Engineering the BirA_{R118G}-biotin ligase into the MHV replicase transcriptase complex**

91 To insert the promiscuous biotin ligase BirA_{R118G} as an integral subunit of the MHV RTC, we
92 used a vaccinia virus-based reverse genetic system (32, 33) to generate a recombinant MHV
93 harboring a myc-tagged BirA_{R118G} fused to nsp2. This strategy was recently employed by
94 Freeman *et al.* for a fusion of green fluorescent protein (GFP) with nsp2 (34). MHV-BirA_{R118G}-
95 nsp2 retained the cleavage site between nsp1 and BirA_{R118G}, while a deleted cleavage site
96 between BirA_{R118G} and nsp2 ensured the expression of a BirA_{R118G}-nsp2 fusion protein (Fig.
97 1a).

98 MHV-BirA_{R118G}-nsp2 replicated to comparable peak titers and replication kinetics as the
99 parental wild-type MHV-A59 (Fig. 1b). MHV-EGFP-nsp2, which was constructed in parallel
100 and contained the coding sequence of EGFP (34) instead of BirA_{R118G}, was used as a control
101 and also reached wild-type virus peak titers, with slightly reduced viral titers at 9 hours post-
102 infection (h.p.i.) compared to MHV-A59 and MHV-BirA_{R118G}-nsp2 (Fig. 1b).

103 To confirm the accommodation of BirA_{R118G} within the viral RTC, MHV-A59-, MHV-
104 BirA_{R118G}-nsp2-, and mock-infected L929 fibroblasts were visualized using indirect
105 immunofluorescence microscopy. BirA_{R118G}-nsp2 remained strongly associated with the MHV
106 RTC, as indicated by the co-localization of BirA_{R118G}-nsp2 with established markers of the
107 MHV replicase, such as nsp2/3 and nsp8 (Fig. 1c; Supplemental Fig. S1). This observation
108 corroborates previous studies demonstrating that nsp2, although not required for viral RNA
109 synthesis, co-localizes with other nsps of the coronaviral RTC (35-37). Importantly, by

110 supplementing the culture medium with biotin, we could readily detect biotinylated proteins
111 with fluorophore-coupled streptavidin that appeared close to the MHV RTC in MHV-
112 BirA_{R118G}-nsp2-infected cells, demonstrating efficient proximity-dependent biotinylation of
113 RTC-proximal host factors (Fig. 1c; Supplemental Fig. S1). Furthermore, to define the
114 localization of the nsp2 fusion protein at the ultrastructural level, we replaced the BirA_{R118G}
115 biotin ligase with the APEX2 ascorbate peroxidase to generate recombinant MHV-APEX2-
116 nsp2. APEX2 mediates the catalysis of 3,3'-diaminobenzidine (DAB) into an insoluble
117 polymer that can be readily observed by electron microscopy (38). As shown in figure 1d,
118 APEX2-catalyzed DAB polymer deposition was readily detectable at characteristic coronavirus
119 replication compartments, such as DMVs and CM, categorically demonstrating that the nsp2
120 fusion proteins localize to known sites of coronavirus replication (4, 8).

121 Importantly, our collective results establish that the recombinant MHV-BirA_{R118G}-nsp2
122 replicates with comparable kinetics to wild-type MHV-A59, expresses a functional BirA_{R118G}
123 biotin ligase that is tightly associated with the MHV RTC, and that biotinylated, RTC-proximal
124 proteins can be readily detected in MHV-BirA_{R118G}-nsp2 infected cells.

125

126 **Determination of the coronavirus RTC-proximal proteome**

127 To further demonstrate the efficiency and specificity of BirA_{R118G}-mediated biotinylation we
128 assessed, by western blot analysis, fractions of biotinylated proteins derived from MHV-A59-
129 , MHV-BirA_{R118G}-nsp2-, or non-infected cells that were grown with or without the addition of
130 biotin (Fig. 2a,b). A characteristic pattern of endogenously biotinylated proteins was observed
131 under all conditions where no exogenous biotin was added to the culture medium (Fig. 2b).
132 The same pattern was detectable in non-infected and wild-type MHV-A59-infected cells when
133 the culture medium was supplemented with biotin, suggesting that the addition of biotin in the

134 absence of the BirA_{R118G} biotin ligase does not recognizably change the fraction of
135 endogenously biotinylated proteins. In contrast, we observed a greatly increased fraction of
136 biotinylated proteins in lysates derived from MHV-BirA_{R118G}-nsp2-infected cells treated with
137 biotin. This result demonstrates that virus-mediated expression of the BirA_{R118G} biotin ligase
138 results in efficient biotinylation when biotin is added to the culture medium. Moreover, we
139 could readily affinity purify, enrich, and recover the fraction of biotinylated proteins under
140 stringent denaturing lysis and washing conditions by using streptavidin-coupled magnetic
141 beads (Fig. 2b).

142 Affinity purified proteins derived from biotin-treated MHV-A59- and MHV-BirA_{R118G}-nsp2-
143 infected cells were subjected to mass spectrometric analysis (n=3). Liquid chromatography
144 tandem-mass spectrometry (LC-MS/MS) was performed from in-gel digested samples and log-
145 transformed label free quantification (LFQ) levels were used to compare protein enrichment
146 between samples (Fig. 2c). Overall, 1381 host proteins were identified, of which 513 were
147 statistically significantly enriched in MHV-BirA_{R118G}-nsp2-infected samples over MHV-A59-
148 infected samples. These host proteins represent a comprehensive repertoire of RTC-proximal
149 factors throughout MHV infection (Fig. 2c, table S1). Importantly, viral replicase gene
150 products nsp2-10 and nsp12-16, and the nucleocapsid protein were significantly enriched in
151 fractions derived from MHV-BirA_{R118G}-nsp2-infected cells (Fig. 2c, d). This is in agreement
152 with studies demonstrating co-localization and interactions amongst individual nsps, and with
153 studies showing association of the nucleocapsid protein with the coronavirus RTC (8, 39-41).
154 It also highlights the specificity and effectiveness of the labeling approach in live cells and is
155 the first experimental evidence showing that collectively these viral nsps and the nucleocapsid
156 (N) protein are subunits of the coronavirus RTC. Furthermore, these results corroborate
157 previous reports that nsp1 is likely not an integral component of the coronavirus RTC (10-12,
158 42). Amongst the “not detected” or “not enriched” viral proteins are (i) nsp11, which is a short

159 peptide of only 14 amino acids at the carboxyterminus of polyprotein 1a with a yet unassigned
160 role or function in coronavirus replication, (ii) the structural proteins spike (S) protein,
161 envelope (E) protein, and membrane (M) protein, which mainly localize to sites of viral
162 assembly before being incorporated into newly-formed viral particles, and (iii) all accessory
163 proteins (NS2a, HE, ORF4, ORF5a). Altogether, these results validate the proximity-
164 dependent biotinylation approach and demonstrate the specific and exclusive labeling of MHV-
165 RTC-associated proteins (Fig. 2d).

166 The BirA_{R118G} biotin ligase biotinylates proteins in its close proximity that must not necessarily
167 have tight, prolonged, or direct interaction (31). Therefore, the identified RTC-proximal host
168 proteins, recorded over the entire duration of the MHV replication cycle, likely include proteins
169 that display a prolonged co-localization with the MHV RTC, proteins that may locate only
170 transiently in close proximity to the RTC, and proteins of which only a minor fraction of the
171 cellular pool may associate with the RTC. To this end, we assessed the localization of a limited
172 number of host proteins from our candidate list in MHV-infected cells. Accordingly, we
173 identified RTC-proximal host proteins displaying a pronounced co-localization with the MHV
174 RTC, such as the ER protein reticulon 4 (rtn4; Fig. 2e), and host proteins where co-localization
175 by indirect immunofluorescence microscopy was not readily detectable, such as the eukaryotic
176 translation initiation factor 3E (eIF3E; Fig. 2e). However, in the latter case, a more sensitive
177 detection technique, such as a proximity ligation assay that relies on proximity-dependent
178 antibody-coupled DNA probe amplification (43), demonstrated proximity of eIF3E and
179 dsRNA in MHV-infected cells (Fig. 2f).

180 Collectively, our results show that the approach of integrating a promiscuous biotin ligase as
181 an integral subunit into a coronavirus RTC revealed a comprehensive list of host cell proteins
182 that comprises the RTC microenvironment. The efficacy and specificity of our approach is best
183 illustrated by the fact that we were able to identify all expected viral components of the MHV

184 RTC, while other viral proteins, such as nsp1, structural proteins S, E, and M, and accessory
185 proteins, were not amongst the significantly enriched proteins. Our data further suggest that
186 the RTC microenvironment may be highly dynamic and likely also contains proteins that are
187 only transiently present in the microenvironment or only comprise a sub-fraction of the cellular
188 pool in close proximity to the MHV RTC.

189

190 **Functional classification of RTC-proximal host factors**

191 To categorize functionally-related proteins from the list of RTC-proximal host proteins and
192 identify enriched biological themes in the dataset, we performed a functional classification of
193 RTC-proximal factors using Gene Ontology (GO) enrichment analysis. 86 GO biological
194 process (BP) terms were significantly enriched in the dataset (p-value <0.05), of which 32
195 terms were highly significant (p-value <0.005) (Fig. 3a, Table S2). Additional analysis using
196 AmiGO revealed that 25 of these 32 highly significant GO BP terms fell into 5 broad functional
197 categories, namely cell adhesion, transport, cell organization, translation, and catabolic
198 processes. To examine these categories further, identify important cellular pathways within
199 them, and extract known functional associations among RTC-proximal host proteins, we
200 performed STRING network analysis on the RTC-proximal proteins in each category (Fig. 3b,
201 c, Fig S2).

202 Despite “cell-cell adhesion” scoring high, it likely represents a typical limitation of gene
203 annotation databases, where many genes play multiple roles in numerous pathways and
204 processes. Accordingly, most genes assigned to the GO BP term cell-cell adhesion are also
205 found in the other categories described below.

206 The category “transport” included protein trafficking and vesicular-mediated transport
207 pathways and comprised the majority of RTC-proximal factors (Fig. 3a, b). Protein interaction

208 network analysis, using STRING, revealed at least 4 distinct clusters of interacting factors
209 within this category (Fig. 3b). Cluster I, protein transport, comprised nuclear transport
210 receptors at nuclear pore complexes, such as importins and transportins. Interestingly, this
211 cluster also contained Sec63, which is part of the Sec61 translocon (44) and has been implicated
212 in protein translocation across ER membranes. The list of RTC-proximal factors also included
213 signal recognition particles SRP54a and SRP68 (Table S2) proteins that promote the transfer
214 of newly synthesized integral membrane proteins or secreted proteins across translocon
215 complexes. Furthermore, the list contained Naca and BTF3, which prevent the translocation of
216 non-secretory proteins towards the ER lumen (45, 46). Interestingly, genome-wide CRISPR
217 screens have identified proteins involved in biosynthesis of membrane and secretory proteins
218 as required for flavivirus replication (29, 30), suggesting similarities between flaviruses and
219 coronaviruses concerning the requirement of ER-associated protein sorting complexes for viral
220 replication.

221 Cluster II included vesicle components, tethers and SNARE (Soluble N-ethylmaleimide-
222 sensitive-factor Attachment protein Receptor) proteins characteristic of the COPII-mediated
223 ER-to-Golgi apparatus anterograde vesicular transport pathway whereas, cluster III contained
224 components of the COPI-related retrograde Golgi-to-ER transport machinery. Moreover,
225 Cluster IV was comprised of proteins that mediate clathrin-coated vesicle (endosomal)
226 transport between the plasma membrane and the trans-Golgi network (TGN), which is also
227 closely associated with the actin cytoskeleton. Together with sorting nexins, cluster IV
228 components can be regarded as regulating late-Golgi trafficking events and interacting with the
229 endosomal system.

230 Many of the cellular processes and host proteins assigned to “transport” (specifically in clusters
231 II-IV) are also listed in the category “cell organization” (Fig. 3a, S2a). However, this category
232 actually extends the importance of vesicular transport as it also contains factors involved in the

233 architecture, organization, and homeostasis of the ER and Golgi apparatus, and the
234 cytoskeleton-supporting these organelles. The prominent appearance of biological processes
235 linked to protein and vesicular transport between the ER and both the cis- and trans-Golgi
236 network, is in agreement with previous findings that have reported the relevance of the early
237 secretory pathway for a number of RNA viruses, including coronaviruses (24, 26, 47-50).

238 Notably, a number of MHV RTC-proximal factors were part of the host translation machinery
239 and assigned to category “translation” (Fig. 3a, c). We found enrichment of factors involved in
240 the initiation of translation, particularly multiple subunits of eIF3 and eIF4 complexes, as well
241 as eIF2, eIF5, the Ddx3y helicase, and the Elongation factor-like GTPase 1, which are required
242 for the formation of 43S pre-initiation complexes, 48S initiation complexes, and the assembly
243 of elongation-competent 80S ribosomes (51). The high degree of interaction between these
244 subunits is suggestive of the presence of the entire translation initiation apparatus in close
245 proximity to the viral RTC. The 60S ribosomal protein L13a (Rp113a), ribosome biogenesis
246 protein RLP24 (Rsl24d1), ribosome-binding protein 1 (Rbp1), release factor Gspt1, and
247 regulatory elements, such as Igf2bp1, Gcn111, Larp, Fam129a and Nck1, are further indicative
248 of the host cell translation machinery near sites of viral RNA synthesis. Notably, our results
249 are in line with a recent genome-wide siRNA screen where translation factors were suggested
250 to play a role in the replication of avian infectious bronchitis coronavirus (IBV) (27). The
251 implication of this finding has, to our knowledge, not been further investigated.

252 Lastly, the category “catabolic processes” (Fig. 3a, S2b) includes a subset of autophagy-related
253 factors and numerous ubiquitin-dependent ERAD components, including the E3 ubiquitin-
254 protein ligase complex and 26S proteasome regulatory subunits (Psmc2, Psmd4). Interestingly,
255 the importance of the ERAD pathway has also been reported in the genome-wide CRISPR
256 screen on flaviviruses, and the ubiquitin-proteasome pathway has been noted to be important
257 for IBV and MHV replication (27, 52).

258 Collectively, the catalogue of coronavirus RTC-proximal proteins greatly expands the
259 repertoire of candidate proteins implicated in the coronavirus replication cycle, and contains
260 several factors that have previously been reported to impact the replication of other positive-
261 sense RNA viruses. Importantly, since our screening approach was tailored to detect host
262 factors associated with the coronavirus RTC, it provides a spatial link of these factors to the
263 site of viral RNA synthesis.

264

265 **Identification of proviral factors within the coronavirus RTC microenvironment**

266 In order to assess the potential functional relevance of RTC-proximal factors identified in our
267 MHV- BirA_{R118G}-nsp2-mediated proximity-dependent screen, we designed a custom siRNA
268 library individually targeting the expression of each of the 513 identified RTC-proximal host
269 proteins. siRNA-treated L929 cells were infected (MOI=0.05, n=4) with a recombinant MHV
270 expressing a *Gaussia* luciferase reporter protein (MHV-Gluc) (53) and replication was assessed
271 by virus-mediated *Gaussia* luciferase expression (Fig. 4a). Cell viability after siRNA
272 knockdown was also assessed and genes resulting in cytotoxicity following silencing were
273 discarded from further analysis. Importantly, we included internal controls of known relevance
274 for MHV entry (MHV receptor Ceacam1a) and replication (Gbf1, Arf1) on each plate and
275 found in each case that siRNA silencing of these factors significantly reduced MHV
276 replication, which underscores the robustness and effectiveness of our approach (Fig. S3a) (24).
277 We found that siRNA-mediated silencing of 53 RTC-proximal host factors significantly
278 reduced MHV replication compared to non-targeting siRNA controls. These factors can
279 therefore be considered proviral and required for efficient replication (Fig. 3b; table S3).
280 Notably, siRNA targets that had the strongest impact on MHV replication were in majority
281 contained within the functional categories highlighted in Fig. 3a (Fig. 4b). Indeed, in line with

282 the hypothesis that MHV subverts key components mediating both anterograde and retrograde
283 vesicular transport between the ER, Golgi apparatus and endosomal compartments for the
284 establishment of replication organelles, several factors contained within these pathways
285 impaired MHV replication as exemplified by the siRNA-mediated silencing of Kif11, Snx9,
286 Dnm11, Scfd1, Ykt6, Stx5a, Clint1, Aak11, or Vapa (Fig. 4b). Consistently, ER-associated
287 protein sorting complexes associated with the ribosome and newly synthesized proteins (Naca,
288 BTF3, SRP54a, SRP68) that were revealed in the GO enrichment analysis (Fig. 3a, table S2),
289 also appear to be required for efficient MHV replication (Fig. 4b).

290 Furthermore, we also observed significantly reduced MHV replication upon silencing of core
291 elements of the 26S and 20S proteasome complex (Psm1 and Psmc2, and Psmb3,
292 respectively), suggesting a crucial role of the ubiquitin-proteasome pathway for efficient CoV
293 replication (27, 52). Indeed, this finding may provide a link to the described coronavirus RTC-
294 encoded de-ubiquitination activity residing in nsp3 that has been implicated in innate immune
295 evasion (16, 17, 54).

296 Most interestingly, this custom siRNA screen identified a crucial role of the host protein
297 synthesis apparatus that was associated with the MHV RTC as indicated by the proximity-
298 dependent proteomic screen (Fig. 3a, c). Silencing of ribosomal proteins Rpl13a and Rls24d1
299 and several subunits of the eIF3 complex resulted in greatly reduced MHV replication and
300 scored with highest significance in the siRNA screen, suggesting that proximity of the host cell
301 translation machinery to the viral RTC likely has functional importance for coronavirus
302 replication (Fig. 4b).

303

304 **Active translation near sites of viral mRNA synthesis**

305 Due to the striking dependence of MHV replication on a subset of RTC-proximal translation
306 initiation factors, we extended these results in independent assays. For this, we selected all host
307 factors assigned to the category “translation” (Fig. 3a) and assessed virus replication following
308 siRNA-mediated silencing of each factor. Measurement of luciferase activity after MHV-Gluc
309 infection confirmed initial findings obtained by screening the entire siRNA library of MHV
310 RTC-proximal factors (Fig. 4c). Specifically for Rpl13a, and eIFs 3i, 3f, and 3e viral replication
311 was reduced to levels comparable to our controls Ceacam1a (MHV receptor) and Gbfl (24).
312 Consistently, cell-associated viral mRNA levels (Fig. 4d) and viral titers (Fig. 4e) were reduced
313 upon siRNA silencing of these factors. Although the silencing of a subset of host translation
314 factors severely restricted MHV replication, effective knockdown of these factors (Fig. S3c)
315 did not affect cell viability (Fig. S3b, d) and only moderately affected host cell translation
316 levels (Fig. 4f, S3e). This data demonstrates that the reduced viral replication observed after
317 siRNA knockdown is not due to a general impairment of host translation.

318 Subsequently, we aimed to visualize the localization of active translation during virus infection
319 by puromycin incorporation into nascent polypeptides on immobilized ribosomes
320 (ribopuromycylation) followed by fluorescence imaging using antibodies directed against
321 puromycin (55). In non-infected L929 cells, ribopuromycylation resulted in an expected
322 diffuse, mainly cytosolic, staining pattern interspersed with punctate structures indicative of
323 translation localized to dedicated subcellular cytosolic locations (Fig. 5). In striking contrast,
324 MHV-infected L929 cells displayed a pronounced enrichment of actively translating ribosomes
325 near the viral RTC as indicated by the strong overlap between the viral replicase and the
326 ribopuromycylation stain. Interestingly, active translation in vicinity of the RTC was strongest
327 during the early phase of infection at 6 h.p.i., and was observed until 8 h.p.i., before gradually
328 decreasing as the infection advanced along with the appearance of typical syncytia formation
329 indicative of cytopathic effect (CPE).

330 Remarkably, we observed a similar phenotype in Huh7 cells infected with human
331 coronaviruses, such as HCoV-229E or the highly pathogenic MERS-CoV (Fig. 6). The HCoV-
332 229E RTC, which was detected with an antiserum directed against nsp8, appeared as small and
333 dispersed perinuclear puncta during early infection and eventually converged into larger
334 perinuclear structures later in infection. Consistent with findings obtained for MHV, we
335 observed a striking co-localization of the HCoV-229E RTC with sites of active translation
336 during the early phase of the infection (Fig. 6, S4). The co-localization gradually decreased as
337 the infection reached the late phase with upcoming signs of CPE. Finally, we further
338 demonstrated that active translation is localized to the site of MERS-CoV RNA synthesis as
339 dsRNA puncta highly overlapped with the ribopuromycylation stain in MERS-CoV-infected
340 Huh7 cells (Fig. 6). Collectively, these results not only confirm the spatial link between
341 individual components of the host cell translation machinery and coronavirus replication
342 compartments as identified by proximity-dependent biotinylation using MHV-BirA_{R118G}-nsp2,
343 but they also demonstrate that active translation is taking place in close proximity to the viral
344 RTC.

345

346 **Discussion**

347 In this study, we made use of a recently developed system based on proximity-dependent
348 biotinylation of host factors in living cells (31). By engineering a promiscuous biotin ligase
349 (BirA_{R118G}) as an integral component of the coronavirus replication complex, we provide a
350 novel approach to define the molecular microenvironment of viral replication complexes that
351 is applicable to many other RNA and DNA viruses.

352 We show that nsp2 fusion proteins encoded by recombinant MHV-APEX2-nsp2 and MHV-
353 BirA_{R118G}-nsp2, are indeed part of the RTC and localize to characteristic coronavirus

354 replicative structures. On the ultrastructural level, APEX2-catalyzed DAB polymer
355 depositions were detected at DMVs and CMs, and we observed co-localization of BirA_{R118G}
356 with established coronavirus RTC markers, such as nsp2/3 and nsp8, by indirect
357 immunofluorescence microscopy. Notably, in MHV-BirA_{R118G}-nsp2-infected cells the
358 detection of biotinylated coronavirus replicase gene products nsp2-10, nsp12-16, and the
359 nucleocapsid protein by mass spectrometry demonstrates that these proteins are in close
360 proximity during infection. This extends previous immunofluorescence and electron
361 microscopic studies that were limited by the availability of nsp-specific antibodies and could
362 only show localization of individual nsps to coronavirus replicative structures (4, 8, 35-37).
363 Moreover, the close proximity of BirA_{R118G}-nsp2 to MHV replicative enzymes, such as the
364 RNA-dependent RNA polymerase (nsp12), the NTPase/helicase (nsp13), the 5'-cap
365 methyltransferases (nsp14, nsp16), the proof-reading exonuclease (nsp14), in MHV-BirA_{R118G}-
366 nsp2-infected cells further suggest close proximity of nsp2 to the site of viral RNA synthesis.
367 We thus propose that nsp2-16 and the nucleocapsid protein collectively constitute a functional
368 coronavirus replication and transcription complex in infected cells.

369 The analysis of the host proteome enriched at MHV replication sites revealed a comprehensive
370 list of host proteins that constitute the coronavirus RTC microenvironment. This included
371 several individual factors and host cell pathways, especially transport mechanisms involving
372 vesicle-mediated trafficking, which have previously been shown to assist coronavirus
373 replication. (24, 26, 27, 49, 52). Moreover, numerous coronavirus RTC-proximal host proteins
374 and pathways also have documented roles in the life cycle of other, more intensively studied,
375 positive-stranded RNA viruses, suggesting considerable commonalities and conserved virus-
376 host interactions at the replication complexes of a broad range of RNA viruses (29, 30, 56).
377 Importantly, our list of RTC-proximal proteins by far exceeds the number of host cell proteins
378 currently known to interact with viral replication complexes and the vast majority of MHV

379 RTC-proximal proteins have not been described before. These likely include proteins with
380 defined temporal roles during particular phases of the viral life cycle and proteins that did not
381 yet attract our attention in previous screens because of functional redundancies. We therefore
382 expect that this approach will find wide application in the field of virus-host interaction, target
383 identification for virus inhibition, and provides a starting point to reveal similarities and
384 differences between replication strategies of a broad range of viruses.

385 One novel finding that arose immediately from our RTC-proximity screen is the demonstration
386 of a close spatial association of host cell translation with the coronavirus RTC. Indeed, the
387 biotin ligase-based proteomic screen identified a number of translation initiation factors, most
388 prominently several eIF3 subunits that were found to have functional importance for viral
389 replication, and numerous ribosome- and translation-associated proteins within the coronavirus
390 RTC microenvironment (Fig. 3, 4). In addition, the presence of subunits of the signal
391 recognition particle in proximity to the coronavirus RTC and their functional relevance for
392 viral replication is indicative of an importance for the translation of membrane proteins.
393 Notably, the coronavirus RTC is translated as two polyproteins that contain nsp3, 4 and 6 with
394 multiple trans-membrane domains that are believed to anchor the RTC at ER-derived
395 membranes (4, 47). It is thus tempting to speculate that the coronavirus RTC is either attracting,
396 or deliberately forming in proximity to, the ER-localized host translation machinery in order
397 to facilitate replicase translation and insertion into ER membranes. This idea is also applicable
398 to many other positive-stranded RNA viruses that express viral polyproteins with embedded
399 trans-membrane domains to anchor the viral replication complex in host endomembranes.
400 Recent experimental evidence for Dengue virus supports this hypothesis. By using cell
401 fractionation and ribosomal profiling it has been shown that translation of the Dengue virus
402 (family *Flaviviridae*) genome is associated with the ER-associated translation machinery
403 accompanied by ER-compartment-specific remodeling of translation (57). Moreover, several

404 recent genome-wide CRISPR screens demonstrated the functional importance of proteins
405 involved in biosynthesis of membrane and secretory proteins, further supporting a pivotal role
406 of the ER-associated translation machinery for virus replication (30).

407 Compartmentalization of cellular translation to sites of viral RNA synthesis has been described
408 for dsRNA viruses of the orthoreovirus family, which replicate and assemble in distinct
409 cytosolic inclusions known as viral factories to which the host translation machinery is
410 recruited (58). The data presented here indicate that coronaviruses have evolved a similar
411 strategy by compartmentalizing and directing viral RNA synthesis to sites of ER-associated
412 translation. Likewise, this strategy has a number of advantages. Coronaviruses would not
413 require sophisticated transport mechanisms that direct viral mRNA to distantly located
414 ribosomes. A close spatial association of viral RNA synthesis and translation during early post-
415 entry events would rather allow for remodeling the ER-associated translation machinery to
416 ensure translation of viral mRNA in a protected microenvironment. Viruses have evolved
417 diverse mechanisms to facilitate translation of their mRNAs including highly diverse internal
418 ribosomal entry sites, recruitment of translation-associated host factors to viral RNAs, and even
419 transcript-specific translation (59, 60). Accordingly, by remodeling defined sites for viral
420 mRNA translation, the repertoire and concentration of translation factors can be restricted to
421 factors needed for translation of these viral mRNAs. A microenvironment that is tailored
422 towards the translational needs of viral mRNAs in proximity to the viral replicase complex
423 would also make virus replication tolerant to host- or virus-induced shut down of translation at
424 distal sites within the cytosol. Finally, proximity of viral mRNA synthesis and translation can
425 also be considered a mechanism to evade cytosolic mRNA decay mechanisms and innate
426 immune sensors of viral RNA.

427 The novel finding of a close association of the host translation machinery with sites of viral
428 RNA synthesis during coronavirus infection exemplifies the power of the MHV-BirA_{R118G}-

429 nsp2 –mediated labelling approach to identify RTC-proximal cellular processes that
430 significantly contribute to viral replication. Indeed, the ability of BirAR_{118G} to label viral and
431 host factors independently of high affinity and prolonged molecular interactions enables the
432 establishment of a comprehensive repertoire reflecting the history of protein association with
433 the viral RTC, recorded during the entire course of infection. In future studies it will be
434 important to provide an “RTC-association map” with temporal resolution. Like we have seen
435 for translation initiation factors in this study, association of host cell proteins with the viral
436 RTC might not persist throughout the entire replication cycle but might be of importance only
437 transiently or during specific phases of the replication cycle. Given its short labelling time,
438 APEX2 indeed offers this possibility to dissect protein recruitment to the viral RTC in a time-
439 resolved manner, i.e. to detect RTC-associated host proteins at specific time points post
440 infection. This will ultimately result in a dynamic, high resolution molecular landscape of
441 virus-host interactions at the RTC and provide an additional impetus to elucidate critical virus-
442 host interactions that take place at the site of viral RNA synthesis. These interactions should
443 be exploited in the development of novel strategies to combat virus infection, based on
444 conserved mechanisms of interactions at replication complexes of a broad range of positive-
445 stranded RNA viruses.

446

447 **Acknowledgements**

448 We thank Mark Denison, Susan Baker, and John Ziebuhr for sharing virus sequence
449 information and antisera. We thank Sandra Huber and Kerry Woods for helpful discussions.

450 This work was supported by the Swiss National Science Foundation (SNF; grants #
451 310030_173085, and # CRSII3_160780 to V.T.). S.P. was supported by the European

452 Commission's Horizon 2020 research and innovation program under the Marie Skłodowska-
453 Curie grant agreement no. 748627.

454

455 **Author Contributions**

456 Conceptualization, P.V., V.T.; Investigation, P.V., M.G., S.P., N.E., S.B.L., J.P., H.P., V.G.,
457 R.D.; Formal Analysis, J.K., S.B.L., C.S., M.H.; Writing – Original Draft, P.V., V.T.;
458 Supervision, V.T., R.D., M.H., R.B., M.S.; Funding Acquisition, V.T., R.D., M.H., R.B., M.S.,
459 S.P.

460

461 **Declaration of Interests**

462 The authors declare no competing interests

463 **Methods**

464 **Cells**

465 Murine L929 fibroblasts (Sigma) and murine 17C11 fibroblasts (gift from S.G. Sawicki) were
466 cultured in MEM supplemented with 10% (v/v) heat-inactivated fetal bovine serum (FBS), 100
467 µg/ml streptomycin and 100 IU/ml penicillin (MEM+/+). Huh-7 hepatocarcinoma cells (gift
468 from V. Lohnmann) and Vero B4 cells (kindly provided by M. Müller) were propagated in
469 Dulbecco's Modified Eagle Medium-GlutaMAX supplemented with, 1 mM sodium pyruvate,
470 10% (v/v) heat-inactivated fetal bovine serum, 100 µg/ml streptomycin, 100 IU/ml penicillin
471 and 1% (w/v) non-essential amino acids.

472

473 **Viruses**

474 Recombinant MHV strain A59 (WT), MHV-Gluc (61), which expresses a *Gaussia* luciferase
475 reporter replacing accessory gene 4 of MHV strain A59, and HCoV-229E were generated as
476 previously described(32, 33, 62). Viruses were propagated on 17C11 cells (MHV) and Huh-7
477 cells (hCoV-229E) and their sequence was confirmed by RT-PCR sequencing. MERS-CoV
478 (63, 64) was propagated and titrated on Vero cells.

479

480 **Generation of recombinant MHV viruses**

481 Recombinant MHV viruses were generated using a vaccinia virus-based system as described
482 before (33). In short, a pGPT-1 plasmid encoding an *Escherichia coli* guanine
483 phosphoribosyltransferase (GPT) flanked by MHV-A59 nt 447-950 and 1315-1774 was used
484 for targeted homologous recombination with a vaccinia virus (VV) containing a full-length
485 cDNA copy of the MHV-A59 genome (32). The resulting GPT-positive VV was further used
486 for recombination with a plasmid containing the EGFP coding sequence flanked by MHV-
487 A59 nt 477-956 and 951-1774 for the generation of MHV-GFP-nsp2, based on the strategy

488 employed by Freeman et al.(34). Alternatively, a plasmid containing the BirA_{R118G} coding
489 sequence (31) or the APEX2 coding sequence (65), with a N-terminal myc-tag or V5-tag,
490 respectively, and a C-terminal (SGG)₃ flexible linker flanked by MHV-A59 nt 477-956 and
491 951-1774 was used for the generation of MHV- BirA_{R118G}-nsp2 and MHV-APEX2-nsp2. The
492 resulting VV were used to generate full-length cDNA genomic fragments by restriction
493 digestion of the VV backbone. Rescue of MHV-GFP-nsp2, MHV-BirA_{R118G}-nsp2 and MHV-
494 APEX2-nsp2 was performed by electroporation of capped *in vitro* transcribed recombinant
495 genomes into a BHK-21-derived cell line stably expressing the nucleocapsid (N) protein
496 layered on permissive 17C11 mouse fibroblasts. Recombinant MHV viruses were plaque-
497 purified three times and purified viruses were passaged three times for stock preparations. All
498 plasmid sequences, VV sequences and recombinant MHV sequences were confirmed by PCR
499 or RT-PCR sequencing. Viruses were propagated on 17C11 cells and virus stocks were titrated
500 by plaque assay on L929 cells.

501

502 **Viral replication assay**

503 L929 cells were infected with MHV-A59, MHV-GFP-nsp2, MHV-BirA_{R118G}-nsp2 or MHV-
504 APEX2-nsp2 in quadruplicate at an MOI=1. Virus inoculum was removed 2 h.p.i., cells were
505 washed with PBS and fresh medium was added. Viral supernatants were collected at the
506 indicated time point and titrated by plaque assay on L929 cells. Titers reported are the averages
507 of three independent experiments \pm standard error of the mean (SEM).

508

509 **Immunofluorescence imaging**

510 Biotinylation assays were carried out as described before with minor modifications(66). 10^6
511 L929 cells grown on glass coverslips were infected with MHV-A59, MHV-BirA_{R118G}-nsp2 or
512 MHV-APEX2-nsp2 at an MOI=1, or non-infected in medium supplemented with 67 μ M biotin

513 (Sigma B4501). Cells were washed three times with PBS at the indicated time points and fixed
514 with 4% (v/v) neutral buffered formalin before being washed three additional times. Cells were
515 permeabilized in PBS supplemented with 50 mM NH₄Cl, 0.1% (w/v) Saponin and 2% (w/v)
516 BSA (CB) for 60 min and incubated 60 min with the indicated primary antibodies diluted in
517 CB (polyclonal anti-MHV-nsp2/3 or nsp8 (gift from S. Baker), 1:200 (35, 67); anti-myc,
518 1:8000 Cell Signalling 2276). Cells were washed three times with CB and incubated for 60 min
519 with donkey-derived, AlexaFluor488-conjugated anti-mouse IgG (H+L) and donkey-derived,
520 AlexaFluor647-conjugated anti-rabbit IgG (H+L) (Jackson ImmunoResearch). Cells were
521 additionally labelled with streptavidin conjugated to AlexaFluor 594 (Molecular Probes) to
522 detect biotinylated proteins. Coverslips were mounted on slides using ProLong Diamond
523 Antifade mountant containing 4',6-diamidino-2-phenylindole (DAPI) (Thermo Fisher
524 Scientific).

525 For indirect immunofluorescence detection of viral and host proteins, L929 cells were grown
526 on glass coverslips in 24-well plates and infected with MHV-A59 or MHV-BirA_{R118G}-nsp2
527 (MOI=1). At the indicated time point, cells were fixed with 4% (v/v) formalin and processed
528 using primary monoclonal antibodies directed against dsRNA (J2 Mab, English Scientific and
529 Consulting) or myc-tab (Cell signalling 2276) and polyclonal antibodies recognizing eIF3E
530 (Sigma, HPA023973) or RTN4 (Nogo A+B, Abcam 47085) as well as secondary donkey-
531 derived, AlexaFluor488-conjugated anti-mouse and AlexaFluor647-conjugated anti-rabbit IgG
532 (H+L), as described above.

533 For proximity ligation assays, L929 cells were seeded in 24-well plates on glass coverslips and
534 infection with MHV-A59 or MHV-BirA_{R118G}-nsp2 (MOI=1). At the indicated time point, cells
535 were washed with PBS, fixed with 4% (v/v) formalin and permeabilized with 0.1% (v/v) Triton
536 X-100. Proximity ligation was performed as recommended by the manufacturer (Duolink In
537 Situ detection reagents Red, Sigma) using monoclonal antibodies directed against dsRNA (J2,

538 English & Scientific Consulting) or myc-tag (Cell Signaling 2276) and polyclonal antibodies
539 recognizing eIF3E (Sigma, HPA023973) or RTN4 (Nogo A+B, Abcam 47085). Coverslips
540 were mounted using Duolink® In Situ Mounting Media with DAPI (Sigma).

541 All samples were imaged by acquiring 0.2 µm stacks over 10 µm using a DeltaVision Elite
542 High-Resolution imaging system (GE Healthcare Life Sciences) equipped with a 60x or 100x
543 oil immersion objective (1.4 NA). Images were deconvolved using the integrated softWoRx
544 software and processed using Fiji (ImageJ).

545

546 **Biotinylation assay – western blot – mass spectrometry**

547 L929 cells were infected with MHV-A59 or MHV-BirA_{R118G}-nsp2, and for comparison
548 MHV_{H277A} and MHV_{H277A}-BirA_{R118G}-nsp2, at an MOI=1 in medium supplemented with 67 µM
549 biotin (Sigma B4501). At 15 h.p.i., cells were washed three times with PBS and lysed in ice-
550 cold buffer containing 50 mM TRIS-Cl pH 7.4, 500 mM NaCl, 0.2% (w/v) SDS, 1 mM DTT
551 and 1x protease inhibitor (cOmplete Mini, Roche). Cells were scraped off the flask and
552 transferred to tubes. Cells were kept on ice until the end of the procedure. Triton X-100 was
553 added to each sample to a final concentration of 2%. Samples were sonicated for two rounds
554 of 20 pulses with a Branson Sonifier 250 (30% constant, 30% power). Equal volumes of 50
555 mM TRIS-Cl were added to each sample and samples were centrifuged at 4 °C for 10 min at
556 18000 x g. Supernatants were incubated with magnetic beads on a rotator at 4 °C overnight
557 (800 µl Dynabeads per sample, MyOne Streptavidin C1, Life Technologies) that were
558 previously washed with lysis buffer diluted 1:1 with 50 mM TRIS-Cl. Beads were washed
559 twice with buffer 1 (2% (w/v) SDS), once with buffer 2 (0.1% (w/v) deoxycholic acid, 1%
560 (v/v) Triton X-100, 1 mM EDTA, 500 mM NaCl, 50 mM HEPES pH 7.5), once with buffer 3
561 (0.5% w/v deoxycholic acid, 0.5% NP40, 1 mM EDTA, 250 mM LiCl, 10 mM TRIS-Cl pH

562 7.4) and once with 50 mM TRIS-Cl pH 7.4. Proteins were eluted from beads by the addition
563 of 0.5 mM biotin and Laemmli SDS-sample buffer and heating at 95 °C for 10 min.
564 For SDS-PAGE and western blot analysis, cells were cultured in 6-well plates and lysates were
565 prepared and affinity purified as described above. Proteins were separated on 10% (w/v) SDS-
566 polyacrylamide gels (Bio-Rad), and proteins were electroblotted on nitrocellulose membranes
567 (Amersham Biosciences, GE Healthcare) in a Mini Trans-Blot cell (Bio-Rad). Membranes
568 were incubated in a protein-free blocking buffer (Advansta) and biotinylated proteins were
569 probed by incubation with horseradish peroxidase-conjugated Streptavidin (Dako). Proteins
570 were visualized using WesternBright enhanced chemiluminescence horseradish peroxidase
571 substrate (Advansta) according to the manufacturer's protocol.
572 For mass spectrometry analysis, lysates and affinity purification were performed as described
573 above from 4×10^7 cells cultured in 150 cm² tissue culture flasks. Proteins were separated 1 cm
574 into a 10% (w/v) SDS-polyacrylamide gel. A Coomassie stain was performed and 4x 2 mm
575 bands were cut with a scalpel. Proteins on gel samples were reduced, alkylated and digested
576 with Trypsin(68). Digests were loaded onto a pre-column (C18 PepMap 100, 5 μ m, 100 A, 300
577 μ m i.d. x 5 mm length) at a flow rate of 20 μ L/min with solvent C (0.05% TFA in
578 water/acetonitrile 98:2). After loading, peptides were eluted in back flush mode onto the
579 analytical Nano-column (C18, 3 μ m, 100 \AA , 75 μ m x 150 mm, Nikkyo Technos C. Ltd., Japan)
580 using an acetonitrile gradient of 5% to 40% solvent B (0.1% (v/v) formic acid in
581 water/acetonitrile 4,9:95) in 40 min at a flow rate of 400 nL/min. The column effluent was
582 directly coupled to a Fusion LUMOS mass spectrometer (Thermo Fischer, Bremen; Germany)
583 via a nano-spray ESI source. Data acquisition was made in data dependent mode with precursor
584 ion scans recorded in the orbitrap with resolution of 120'000 (at m/z=250) parallel to top speed
585 fragment spectra of the most intense precursor ions in the Linear trap for a cycle time of 3
586 seconds maximum. Spectra interpretation was performed with Easyprot on a local, server run

587 under Ubuntu against a forward + reverse *Mus musculus* (UniprotKB version 2016_04) and
588 MHV (UniprotKB version 2016_07) database, using fixed modifications of
589 carboamidomethylated on Cysteine, and variable modification of oxidation on Methionine,
590 biotinylation on Lysine and on protein N-term, and deamidation of Glutamine and Asparagine.
591 Parent and fragment mass tolerances were set to 10 ppm and 0.4 Da, respectively. Matches on
592 the reversed sequence database were used to set a Z-score threshold, where 1% false
593 discoveries (FDR) on the peptide spectrum match level had to be expected. Protein
594 identifications were only accepted, when two unique peptides fulfilling the 1% FDR criterion
595 were identified. MS identification of biotinylated proteins was performed in three independent
596 biological replicates. For label-free protein quantification, LC-MS/MS data was interpreted
597 with MaxQuant (version 1.5.4.1) using the same protein sequence databases and search
598 parameters as for EasyProt. Match between runs was activated, however samples from different
599 treatments were given non-consecutive fraction numbers in order to avoid over-interpretation
600 of data. The summed and median normalized top3 peptide intensities extracted from the
601 evidence table as a surrogate of protein abundance (69) and LFQ values were used for statistical
602 testing. The protein groups were first cleared from all identifications, which did not have at
603 least two valid LFQ values. Protein LFQ levels derived from MaxQuant were log-transformed.
604 Missing values were imputed by assuming a normal distribution between sample replicates. A
605 two-tailed t-test was used to determine significant differences in protein expression levels
606 between sample groups and p-values were adjusted for multiple testing using the Benjamini-
607 Hochberg (FDR) test.

608

609 **Computational analysis**

610 Database for Annotation, Visualization, and Integrated Discovery (DAVID) was used to
611 perform GO enrichment analysis on the RTC-proximal cellular factors identified via mass

612 spectrometry(70-73). GO BP terms with a p-value <0.05 were considered to be terms that were
613 significantly enriched in the dataset. Additional analysis of significant GO terms was conducted
614 using AmiGO and revealed that the top 32 GO BP terms (p-value <0.005) were predominantly
615 associated with five broad functional categories (cell-cell adhesion, transport, cell organization,
616 translation, and catabolic processes)(74). Alternatively, enrichment analysis was performed
617 using SetRank (data not shown), a recently described algorithm that circumvents pitfalls of
618 commonly used approaches and thereby reduces the amount of false-positive hits (75) and the
619 following databases were searched for significant gene sets: BIOCYC (76), GO (72), ITPF
620 (77), KEGG (78), PhosphoSitePlus (79), REACTOME (80), and WikiPathways (81). Both
621 independent approaches lead to highly similar results and consistently complement results
622 obtained upon GO Cellular Components analysis.

623 STRING functional protein association networks were generated using RTC-proximal host
624 proteins found within each of the five broad functional categories. Default settings were used
625 for active interaction sources and a high confidence interaction score (0.700) was used to
626 maximize the strength of data support. The MCL clustering algorithm was applied to each
627 STRING network using an inflation parameter of 3 (82, 83).

628

629 **siRNA screen**

630 A custom siRNA library targeting each individual RTC-proximal factor (On Target Plus,
631 SMART pool, 96-well plate format, Dharmacon, GE Healthcare) was ordered. 10 nM siRNA
632 were reverse transfected into L929 cells (8×10^3 cells per well) using Viromer Green
633 (Lipocalyx) according to the manufacturer's protocol. Cells were incubated 48 hours at 37 °C
634 5% CO₂ and cell viability was assessed using the CytoTox 96[®] Non-Radioactive Cytotoxicity
635 Assay (Promega). Cells were infected with MHV-Gluc (MOI=0.05, 1000 plaque forming
636 units/well), washed with PBS 3 h.p.i. and incubated in MEM+/+ for additional 12 hours.

637 Gaussia luciferase was measured from the supernatant using Pierce™ Gaussia Luciferase Glow
638 Assay Kit (ThermoFisher Scientific). Experiments were carried out in 4 independent replicates
639 and both cytotoxicity values and luciferase counts were normalized to the corresponding non-
640 targeting scrambled control of each plate. A one-way ANOVA (Kruskal-Wallis test,
641 uncorrected Dunn's test) was used to test the statistical significance of reduced viral replication
642 (mean < 95% as compared to scramble control, n=216). The R package ggplot2 was used to
643 create the bubble plot (Fig 4B).

644

645 **siRNA screen validation**

646 L929 cells were transfected with 10 nM siRNA as described above. 48 h post-transfection, cell
647 viability was assessed using the CytoTox 96® Non-Radioactive Cytotoxicity Assay (Promega)
648 and visually inspected by automated phase-contrast microscopy using an EVOS FL Auto 2
649 Imaging System equipped with a 4x air objective. Cells were infected with MHV-Gluc
650 (MOI=0.05), washed with PBS 3 h.p.i. and incubated for 9 additional hours. *Gaussia* luciferase
651 activity, viral titers and cell viability were measured from the supernatant as described above.
652 One-way ANOVAs (ordinary one-way ANOVA, uncorrected Fisher's LSD test) were used to
653 test the statistical significance.

654 Total cellular RNA was isolated from cells using the NucleoMag® RNA Kit (Machery Nagel,
655 Switzerland) on a KingFisher™ Flex Purification System (Thermo Fisher Scientific,
656 Switzerland) according to the manufacture's instructions. The QuantiTect Probe RT-PCR Kit
657 (Qiagen, Switzerland) was used according to the manufactures instructions for measuring the
658 cell associated viral RNA levels with primers and probe specific to the MHV genome fragment
659 coding the nucleocapsid gene (Table S4). Primers and Probe for mouse Glyceraldehyde 3-
660 phosphate dehydrogenase (GAPDH) where obtained from ThermoFisher Scientific
661 (Mm03302249_g1, Catalog Number: 4331182). The MHV levels were normalized to GAPDH

662 and shown as $\Delta\Delta\text{Ct}$ over mock (ΔCt values calculated as $\text{Ct reference} - \text{Ct target}$). The
663 QuantiTect SYBR® Green RT-PCR Kit (Qiagen, Switzerland) was used according to the
664 manufactures instructions for measuring the expression levels of Rpl13a, eIF3E, eIF3I, eIF3F,
665 eIF4G1, eIF4G2, eIF2ak3, Rsl24d1 and Tbp. All primer pairs where placed over an exon intron
666 junction (Table S4). All expression levels are displayed as $\Delta\Delta\text{Ct}$ over non-targeting siRNA
667 (ΔCt values calculated as $\text{Ct target} - \text{Ct Tbp}$) (84). One-way ANOVA (ordinary one-way
668 ANOVA, uncorrected Fisher's LSD test) was used to test the statistical significance.

669

670 **Total cellular translation**

671 siRNA-based silencing was performed as described above. 48 h post-transfection, control cells
672 were incubated with 355 μM cycloheximide (Sigma) and 208 μM Emetin (Sigma) for 30 min
673 to block protein synthesis. Cells were treated with 3 μM puromycin for 60 min followed by
674 three PBS washes(85). Total cell lysates were prepared using M-PER mammalian protein
675 extraction reagent (Thermo Scientific) supplemented with protease inhibitors (cOmplete Mini,
676 Roche). Lysates were separated on a 10% (w/v) SDS-PAGE and electroblotted as described
677 above. Western blots were probed using a monoclinal AlexaFluor647-conjugated anti-
678 puromycin antibody (clone 12D10, Merk Millipore) and a donkey-derived HRP-conjugated
679 anti-mouse (Jackson immunoresearch 715-035-151). Actin was detected using a monoclonal
680 HRP-conjugated anti-actin antibody (Sigma A3854) and used to normalize input.

681

682 **Ribopuromylation assay**

683 Ribopuromylation of actively translating ribosomes was performed as described before (55).
684 L929, Huh-7 cells were seeded on glass coverslips and infected with MHV-A59 (L929),
685 HCoV-229E (Huh-7), MERS-CoV (Huh-7) and at $\text{MOI}=1$. One hour after inoculation, cells
686 were washed with PBS and incubated further for the indicated time. Cells were treated with

687 355 μ M cycloheximide and 208 μ M Emetin (Sigma) for 15 min at 37°C. Cells were further
688 incubated in medium containing 355 μ M cycloheximide, 208 μ M Emetin and 182 μ M
689 puromycin (Sigma) for additional 5 min. Cells were washed twice in ice-cold PBS and fix on
690 ice for 20 min in buffer containing 50 mM TRIS HCl, 5 mM MgCl₂, 25 mM KCl, 355 μ M
691 cycloheximide, 200 mM NaCl, 0.1% (v/v) TritonX-100, 3% formalin and protease inhibitors
692 (cOmplete Mini, Roche). Cells were blocked for 30 min in CB, and immunostained as
693 described above using polyclonal anti-MHV-nsp2/3 (gift from S. Baker), polyclonal anti-
694 HCoV-229E-nsp8 (gift from J. Ziebuhr), or monoclonal anti-dsRNA (J2 MAB, English and
695 Scientific Consulting) as primary antibodies to detect MHV, HCoV-229E and ZIKV
696 replication complexes, respectively. Donkey-derived, AlexaFluor488-conjugated anti-mouse
697 or anti-rabbit IgG (H+L) were used as secondary antibodies. Additionally, ribosome-bound
698 puromycin was detected using a monoclonal AlexaFluor647-conjugated anti-puromycin
699 antibody (clone 12D10, Merk Millipore). Slides were mounted, imaged and processed as
700 described above.

701

702 **DAB staining and transmission electron microscopy**

703 L929 fibroblasts were seeded in 24-well plates and infected with MHV-APEX2-nsp2, MHV-
704 A59, or non-infected for 10 h. 3,3-diaminobenzidine (DAB) stains were performed as described
705 previously (38). Briefly, cells were fixed at 10 h.p.i. using warm 2% (v/v) glutaraldehyde in
706 100 mM sodium cacodylate, pH 7.4, supplemented with 2 mM calcium chloride (cacodylate
707 buffer) and placed on ice for 60 min. The following incubations were performed on ice in ice-
708 cold buffers unless stated otherwise. Cells were washed 3x with sodium cacodylate buffer,
709 quenched with 20 mM glycine in cacodylate buffer for 5 min. before 3 additional washes with
710 cacodylate buffer. Cells were stained in cacodylate buffer containing 0.5 mg/ml DAB and 10
711 mM H₂O₂ for 20 min until DAB precipitates were visible by light microscopy. Cells were

712 washed 3x with cacodylate buffer to stop the staining reaction. Processing of samples for
713 transmission electron microscopy (TEM) was performed as described previously (86). Briefly,
714 cells were washed once with PBS prewarmed to 37 °C and subsequently fixed with 2.5% (v/v)
715 glutaraldehyde (Merck, Darmstadt, Germany) in 0.1 M cacodylate buffer (Merck, Hohenbrunn,
716 Germany) pH 7.4 for 30 min at room temperature or overnight at 4 °C. After three washes in
717 cacodylate buffer for 10 min each, cells were post-fixed with 1% OsO₄ (Chemie Brunschwig,
718 Basel, Switzerland) in 0.1 M cacodylate buffer for 1 h at 4 °C and again washed three times
719 with cacodylate buffer. Thereafter, cells were dehydrated in an ascending ethanol series (70%,
720 80%, 90%, 94%, 100% (v/v) for 20 min each) and embedded in Epon resin, a mixture of Epoxy
721 embedding medium, dodecenyl succinic anhydride (DDSA) and methyl nadic anhydride
722 (MNA) (Sigma Aldrich, Buchs, Switzerland). Ultrathin sections of 90 nm were then obtained
723 with diamond knives (Diatome, Biel, Switzerland) on a Reichert-Jung Ultracut E (Leica,
724 Heerbrugg, Switzerland) and collected on collodion-coated 200-mesh copper grids (Electron
725 Microscopy Sciences, Hatfield, PA, USA). Sections were double-stained with 0.5% (w/v)
726 uranyl acetate for 30 min at 40 °C (Sigma Aldrich, Steinheim, Germany) and 3% (w/v) lead
727 citrate for 10 min at 20 °C (Laurylab, Saint Fons, France) in an Ultrastain® (Leica, Vienna,
728 Austria) and examined with a Philips CM12 transmission electron microscope (FEI,
729 Eindhoven, The Netherlands) at an acceleration voltage of 80 kV. Micrographs were captured
730 with a Mega View III camera using the iTEM software (version 5.2; Olympus Soft Imaging
731 Solutions GmbH, Münster, Germany).

732

733 **Figure legends**

734 **Figure 1. Characterization of the recombinant MHV-BirA_{R118G}-nsp2.** (a) Genome
735 organization of recombinant MHV-BirA_{R118G}-nsp2. The positive-sense RNA genome of MHV
736 contains a 5' cap and a 3' poly(A) tail. ORF1a and ORF1b encode the viral replication and
737 transcription complex (nsp1-16). myc-BirA_{R118G} was inserted as an N-terminal fusion with
738 nsp2 within ORF1a. The cleavage site between nsp1 and myc-BirA_{R118G} was retained (black
739 arrow) while a deleted cleavage site between BirA_{R118G} and nsp2 ensured the release of a
740 BirA_{R118G}-nsp2 fusion protein from the pp1a polyprotein. The cleavage site between nsp2 and
741 nsp3 was also retained. (b) Viral replication kinetics of recombinant MHV-BirA_{R118G}-nsp2
742 were compared to wild-type MHV-A59 and recombinant MHV-GFP-nsp2. Murine L929
743 fibroblasts were infected at a multiplicity of infection (MOI) of 1 plaque forming unit (pfu) per
744 cell. Viral supernatants were collected at the indicated time points, titrated by plaque assay and
745 expressed in pfu per ml. Data points represent the mean and SEM of three independent
746 experiments, each performed in quadruplicate. (c) Immunofluorescence analysis of MHV-
747 BirA_{R118G}-nsp2-mediated biotinylation of RTC-proximal factors. L929 cells were infected with
748 MHV-BirA_{R118G}-nsp2 (MOI=1) in medium supplemented with 67μM biotin. Cells were fixed
749 15 hours post infection (h.p.i.) and processed for immunofluorescence analysis with antibodies
750 directed against the BirA_{R118G} (anti-myc), the viral replicase (anti-nsp2/3) and biotinylated
751 factors (streptavidin). Nuclei are counterstained with DAPI. Z-projection of deconvolved z-
752 stacks acquired with a DeltaVision Elite High-Resolution imaging system are shown. Scale
753 bars: 20 μm. (d) Ultrastructural analysis of MHV-APEX2-nsp2 infection. L929 cells were
754 infected with MHV-APEX2-nsp2 and MHV-A59 (MOI=2), or mock infected. At 10 h.p.i.,
755 cells were fixed, stained with DAB and processed for electron microscopy investigations.
756 Representative low and high magnifications are displayed.

757

758 **Figure 2. Determination of the coronavirus RTC-proximal proteome** (a) Schematic
759 overview of the BirA_{R118G}-mediated proximity biotinylation assay using MHV-BirA_{R118G}-
760 nsp2. (b) Western blot analysis of MHV-BirA_{R118G}-nsp2-infected L929 cells. L929 cells were
761 infected with MHV-BirA_{R118G}-nsp2, MHV-A59 (parental wild-type strain) or non-infected in
762 medium with and without supplementation of 67 μ M biotin. Cells were lysed 15 h.p.i. and
763 biotinylated factors were subjected to affinity purification using streptavidin-coupled magnetic
764 beads. Total cell lysates and affinity-purified fractions were separated by SDS-PAGE and
765 analysed by western blot probed with horse radish peroxidase (HRP)-coupled Streptavidin. (c)
766 Host and viral factors identified by LC-MS/MS. 4*10⁷ L929 cells were infected with MHV-
767 BirA_{R118G}-nsp2 or MHV-A59 in medium supplemented with 67 μ M biotin. 15 h.p.i., lysates
768 were affinity purified and LC-MS/MS was performed from in-gel digested samples. MS
769 identification of biotinylated proteins was performed in three independent biological replicates.
770 Spectral interpretation was performed against a *Mus musculus* and MHV database and log₂-
771 transformed LFQ levels (x-axis) were used to determine significant differences in protein
772 enrichment between sample groups (Student's T-test, y-axis). Identified cellular proteins are
773 displayed as black dots, MHV proteins are highlighted in red (nsp: non-structural protein, N:
774 nucleocapsid, S: spike, M: membrane, 2a: accessory protein 2a). (d) Summary of viral proteins
775 identified by LC-MS/MS. nsp2-10, nsp12-16, and nucleocapsid were significantly enriched in
776 fractions derived from MHV-BirA_{R118G}-nsp2-infected cells whereas nsp1, nsp11, structural
777 proteins spike (S), envelope (E) and membrane proteins (M) as well as all accessory proteins
778 (NS2a, HE, ORF4, ORF5a) were either not significantly enriched or not detected. (e,f)
779 Immunofluorescence analysis of RTC-proximal cellular factors. L929 cells were seeded on
780 coverslips, infected with MHV-BirA_{R118G}-nsp2 (e) or MHV-A59 (f), fixed at 9 h.p.i. and
781 processed for immunofluorescence using anti-myc, anti-RTN4 and anti-eIF3E antibodies (e)
782 or anti-dsRNA, anti-RTN4 and anti-eIF3E antibodies (f). Secondary fluorophore-coupled

783 antibodies were used to detect the viral replicase and endogenous levels of RTN4 and eIF3E
784 (e). Proximity ligations were performed using Duolink In Situ detection reagents (f). Nuclei
785 are counterstained with DAPI. Z-projection of deconvolved z-stacks acquired with a
786 DeltaVision Elite High-Resolution imaging system are shown. Intensity profiles highlighted in
787 the magnified regions are shown. Scale bars: 20 μ m.

788

789 **Figure 3. Functional classification of RTC-proximal host factors** (a) Gene Ontology
790 enrichment analysis of RTC-proximal cellular factors. 32 terms were highly significant (p-
791 value <0.005) and were assigned to 5 broad functional categories: cell-cell adhesion, transport,
792 cell organization, translation, catabolic processes. (b-c) STRING protein interaction network
793 analysis of the categories “transport” (b) and “translation” (c). The nodes represent RTC-
794 proximal host proteins and the edges represent the interactions, either direct (physical) or
795 indirect (functional), between two proteins in the network. Cellular proteins assigned to the
796 “transport” category separated into 4 distinct interaction clusters. I: protein transport, II: COPII
797 anterograde transport, III: COPI retrograde transport, IV: clathrin-mediated transport.

798

799 **Figure 4. Identification of proviral factors within the coronavirus RTC**
800 **microenvironment** (a) Impact of siRNA-silencing of RTC-proximal cellular proteins on viral
801 replication. L929 fibroblasts were reverse-transfected with siRNAs (10 nM) for 48 h before
802 being infected with MHV-Gluc (MOI=0.05, n=4). Replication was assessed by virus-mediated
803 Gaussia luciferase expression at 15 h.p.i. and was normalized to levels of viral replication in
804 cells targeted by scrambled siRNA controls. Target proteins to the left of the dashed line
805 represent RTC-proximal factors whose silencing decreased viral replication. (b) Bubble plot
806 illustrating host proteins that significantly impact MHV replication. Bubble size is proportional

807 to the level of viral replication impairment. Colors correspond to the functional categories
808 highlighted in Figure 3. Light grey bubbles (below the dashed line) represent host proteins that
809 did not significantly impact MHV replication (p -value > 0.05). (c, d, e, f) Silencing of RTC-
810 proximal components of the cellular translation machinery. Upon 48h siRNA silencing of
811 factors assigned to the category “translation” (Figure 3), L929 fibroblasts were infected with
812 MHV-Gluc (MOI=0.05, n=3). Luciferase activity (c), cell-associated viral RNA levels (d) and
813 viral titers (e) were assessed at 12 h.p.i.. (f) Western blot quantification of total cellular
814 translation following silencing of a subset of the host translation apparatus. Upon 48h siRNA-
815 silencing, L929 fibroblasts were pulsed with 3 μ M puromycin for 60 min. Control cells were
816 treated, prior to puromycin incubation, with 355 μ M cycloheximide and 208 μ M Emetin for
817 30 min to block protein synthesis. Cell lysates were separated by SDS-PAGE and Western
818 blots were probed using anti-puromycin antibodies to assess puromycin incorporation into
819 polypeptides and normalized to actin levels. Error bars represent the mean \pm standard deviation,
820 where * is $p \leq 0.05$, ** is $p \leq 0.005$, *** is $p \leq 0.0005$ and **** is $p < 0.0001$.

821

822 **Figure 5. Active translation near sites of MHV mRNA synthesis.** Visualization of active
823 translation in MHV-infected L929 fibroblasts. Cells infected with MHV-A59 (MOI=1) or non-
824 infected cells were cultured for 6, 8, 10 and 12 hours and pulsed with cycloheximide, emetine
825 and puromycin for 5 min to label translating ribosomes. All cells, including non-treated control
826 infections, were subjected to a coextraction/fixation procedure to remove free puromycin. Cells
827 were labelled using anti-nsp2/3 antiserum and anti-puromycin antibodies. Nuclei are
828 counterstained with DAPI. Z-projection of deconvolved z-stacks acquired with a DeltaVision
829 Elite High-Resolution imaging system are shown. Note the gradual decrease of overlap
830 between the viral replication and actively translating ribosomes highlighted in the intensity
831 profiles. Scale bar: 20 μ m.

832

833 **Figure 6. Active translation near sites of HCoV-229E and MERS-CoV mRNA synthesis.**

834 Visualization of active translation during hCoV-229E and MERS-CoV infections. Huh7 cells
835 were infected with HCoV-229E and MERS-CoV (MOI=1) for 12 h and 6 h, respectively. Cells
836 were pulsed with cycloheximide, emetine and puromycin for 5min to label translating
837 ribosomes and subjected to a coextraction/fixation procedure to remove free puromycin. Non-
838 infected and/or non-pulsed cells were used as control. Cells were labelled using anti-nsp8
839 (HCoV-229E) or dsRNA (MERS-CoV) and anti-puromycin antibodies. Nuclei are
840 counterstained with DAPI. Z-projection of deconvolved z-stacks acquired with a DeltaVision
841 Elite High-Resolution imaging system are shown. Intensity profiles of magnified regions are
842 shown. Scale bar: 20 μ m.

843

844 References

- 845 1. Romero-Brey I & Bartenschlager R (2016) Endoplasmic Reticulum: The Favorite Intracellular
846 Niche for Viral Replication and Assembly. *Viruses* 8(6).
- 847 2. Romero-Brey I, *et al.* (2012) Three-dimensional architecture and biogenesis of membrane
848 structures associated with hepatitis C virus replication. *PLoS Pathog* 8(12):e1003056.
- 849 3. Cortese M, *et al.* (2017) Ultrastructural Characterization of Zika Virus Replication Factories.
850 *Cell Rep* 18(9):2113-2123.
- 851 4. Knoops K, *et al.* (2008) SARS-coronavirus replication is supported by a reticulovesicular
852 network of modified endoplasmic reticulum. *PLoS Biol* 6(9):e226.
- 853 5. Miorin L, *et al.* (2013) Three-dimensional architecture of tick-borne encephalitis virus
854 replication sites and trafficking of the replicated RNA. *J Virol* 87(11):6469-6481.
- 855 6. Overby AK, Popov VL, Niedrig M, & Weber F (2010) Tick-borne encephalitis virus delays
856 interferon induction and hides its double-stranded RNA in intracellular membrane vesicles. *J*
857 *Virol* 84(17):8470-8483.
- 858 7. Neufeldt CJ, *et al.* (2016) The Hepatitis C Virus-Induced Membranous Web and Associated
859 Nuclear Transport Machinery Limit Access of Pattern Recognition Receptors to Viral
860 Replication Sites. *PLoS Pathog* 12(2):e1005428.
- 861 8. Ulasli M, Verheije MH, de Haan CA, & Reggiori F (2010) Qualitative and quantitative
862 ultrastructural analysis of the membrane rearrangements induced by coronavirus. *Cell*
863 *Microbiol* 12(6):844-861.
- 864 9. Oudshoorn D, *et al.* (2017) Expression and Cleavage of Middle East Respiratory Syndrome
865 Coronavirus nsp3-4 Polyprotein Induce the Formation of Double-Membrane Vesicles That
866 Mimic Those Associated with Coronaviral RNA Replication. *MBio* 8(6).
- 867 10. Huang C, *et al.* (2011) SARS coronavirus nsp1 protein induces template-dependent
868 endonucleolytic cleavage of mRNAs: viral mRNAs are resistant to nsp1-induced RNA cleavage.
869 *PLoS Pathog* 7(12):e1002433.
- 870 11. Zust R, *et al.* (2007) Coronavirus non-structural protein 1 is a major pathogenicity factor:
871 implications for the rational design of coronavirus vaccines. *PLoS Pathog* 3(8):e109.
- 872 12. Lokugamage KG, *et al.* (2015) Middle East Respiratory Syndrome Coronavirus nsp1 Inhibits
873 Host Gene Expression by Selectively Targeting mRNAs Transcribed in the Nucleus while
874 Sparing mRNAs of Cytoplasmic Origin. *J Virol* 89(21):10970-10981.
- 875 13. Thiel V, *et al.* (2003) Mechanisms and enzymes involved in SARS coronavirus genome
876 expression. *J Gen Virol* 84(Pt 9):2305-2315.
- 877 14. Snijder EJ, *et al.* (2003) Unique and conserved features of genome and proteome of SARS-
878 coronavirus, an early split-off from the coronavirus group 2 lineage. *J Mol Biol* 331(5):991-
879 1004.
- 880 15. Decroly E, *et al.* (2008) Coronavirus nonstructural protein 16 is a cap-0 binding enzyme
881 possessing (nucleoside-2'-O)-methyltransferase activity. *J Virol* 82(16):8071-8084.
- 882 16. Barretto N, *et al.* (2005) The papain-like protease of severe acute respiratory syndrome
883 coronavirus has deubiquitinating activity. *J Virol* 79(24):15189-15198.
- 884 17. Lindner HA, *et al.* (2005) The papain-like protease from the severe acute respiratory syndrome
885 coronavirus is a deubiquitinating enzyme. *J Virol* 79(24):15199-15208.
- 886 18. Athmer J, *et al.* (2017) In Situ Tagged nsp15 Reveals Interactions with Coronavirus
887 Replication/Transcription Complex-Associated Proteins. *MBio* 8(1).
- 888 19. Kindler E, *et al.* (2017) Early endonuclease-mediated evasion of RNA sensing ensures efficient
889 coronavirus replication. *PLoS Pathog* 13(2):e1006195.
- 890 20. Zust R, *et al.* (2011) Ribose 2'-O-methylation provides a molecular signature for the distinction
891 of self and non-self mRNA dependent on the RNA sensor Mda5. *Nat Immunol* 12(2):137-143.
- 892 21. Eckerle LD, Lu X, Sperry SM, Choi L, & Denison MR (2007) High fidelity of murine hepatitis virus
893 replication is decreased in nsp14 exoribonuclease mutants. *J Virol* 81(22):12135-12144.

- 894 22. Deng X, *et al.* (2017) Coronavirus nonstructural protein 15 mediates evasion of dsRNA sensors
895 and limits apoptosis in macrophages. *Proc Natl Acad Sci U S A* 114(21):E4251-E4260.
- 896 23. Zhang R, *et al.* (2015) The nsp1, nsp13, and M proteins contribute to the hepatotropism of
897 murine coronavirus JHM.WU. *J Virol* 89(7):3598-3609.
- 898 24. Verheije MH, *et al.* (2008) Mouse hepatitis coronavirus RNA replication depends on GBF1-
899 mediated ARF1 activation. *PLoS Pathog* 4(6):e1000088.
- 900 25. Reggiori F, *et al.* (2010) Coronaviruses Hijack the LC3-I-positive EDEMosomes, ER-derived
901 vesicles exporting short-lived ERAD regulators, for replication. *Cell Host Microbe* 7(6):500-508.
- 902 26. de Wilde AH, *et al.* (2015) A Kinome-Wide Small Interfering RNA Screen Identifies Proviral and
903 Antiviral Host Factors in Severe Acute Respiratory Syndrome Coronavirus Replication,
904 Including Double-Stranded RNA-Activated Protein Kinase and Early Secretory Pathway
905 Proteins. *J Virol* 89(16):8318-8333.
- 906 27. Wong HH, *et al.* (2015) Genome-Wide Screen Reveals Valosin-Containing Protein Requirement
907 for Coronavirus Exit from Endosomes. *J Virol* 89(21):11116-11128.
- 908 28. Pfefferle S, *et al.* (2011) The SARS-coronavirus-host interactome: identification of cyclophilins
909 as target for pan-coronavirus inhibitors. *PLoS Pathog* 7(10):e1002331.
- 910 29. Marceau CD, *et al.* (2016) Genetic dissection of Flaviviridae host factors through genome-scale
911 CRISPR screens. *Nature* 535(7610):159-163.
- 912 30. Zhang R, *et al.* (2016) A CRISPR screen defines a signal peptide processing pathway required by
913 flaviviruses. *Nature* 535(7610):164-168.
- 914 31. Roux KJ, Kim DI, Raida M, & Burke B (2012) A promiscuous biotin ligase fusion protein
915 identifies proximal and interacting proteins in mammalian cells. *J Cell Biol* 196(6):801-810.
- 916 32. Coley SE, *et al.* (2005) Recombinant mouse hepatitis virus strain A59 from cloned, full-length
917 cDNA replicates to high titers in vitro and is fully pathogenic in vivo. *J Virol* 79(5):3097-3106.
- 918 33. Eriksson KK, Makia D, & Thiel V (2008) Generation of recombinant coronaviruses using
919 vaccinia virus as the cloning vector and stable cell lines containing coronaviral replicon RNAs.
920 *Methods Mol Biol* 454:237-254.
- 921 34. Freeman MC, Graham RL, Lu X, Peek CT, & Denison MR (2014) Coronavirus Replicase-Reporter
922 Fusions Provide Quantitative Analysis of Replication and Replication Complex Formation. *J*
923 *Virol*.
- 924 35. Schiller JJ, Kanjanahaluethai A, & Baker SC (1998) Processing of the coronavirus MHV-JHM
925 polymerase polyprotein: identification of precursors and proteolytic products spanning 400
926 kilodaltons of ORF1a. *Virology* 242(2):288-302.
- 927 36. Hagemeyer MC, *et al.* (2010) Dynamics of coronavirus replication-transcription complexes. *J*
928 *Virol* 84(4):2134-2149.
- 929 37. Graham RL, Sims AC, Brockway SM, Baric RS, & Denison MR (2005) The nsp2 replicase proteins
930 of murine hepatitis virus and severe acute respiratory syndrome coronavirus are dispensable
931 for viral replication. *J Virol* 79(21):13399-13411.
- 932 38. Martell JD, Deerinck TJ, Lam SS, Ellisman MH, & Ting AY (2017) Electron microscopy using the
933 genetically encoded APEX2 tag in cultured mammalian cells. *Nat Protoc* 12(9):1792-1816.
- 934 39. Denison MR, *et al.* (1999) The putative helicase of the coronavirus mouse hepatitis virus is
935 processed from the replicase gene polyprotein and localizes in complexes that are active in
936 viral RNA synthesis. *J Virol* 73(8):6862-6871.
- 937 40. Sims AC, Ostermann J, & Denison MR (2000) Mouse hepatitis virus replicase proteins associate
938 with two distinct populations of intracellular membranes. *J Virol* 74(12):5647-5654.
- 939 41. van der Meer Y, *et al.* (1999) Localization of mouse hepatitis virus nonstructural proteins and
940 RNA synthesis indicates a role for late endosomes in viral replication. *J Virol* 73(9):7641-7657.
- 941 42. Denison MR, *et al.* (1992) Intracellular processing of the N-terminal ORF 1a proteins of the
942 coronavirus MHV-A59 requires multiple proteolytic events. *Virology* 189(1):274-284.
- 943 43. Soderberg O, *et al.* (2006) Direct observation of individual endogenous protein complexes in
944 situ by proximity ligation. *Nat Methods* 3(12):995-1000.

- 945 44. Rapoport TA (2007) Protein translocation across the eukaryotic endoplasmic reticulum and
946 bacterial plasma membranes. *Nature* 450(7170):663-669.
- 947 45. Wiedmann B, Sakai H, Davis TA, & Wiedmann M (1994) A protein complex required for signal-
948 sequence-specific sorting and translocation. *Nature* 370(6489):434-440.
- 949 46. Gamerding M, Hanebuth MA, Frickey T, & Deuerling E (2015) The principle of antagonism
950 ensures protein targeting specificity at the endoplasmic reticulum. *Science* 348(6231):201-207.
- 951 47. Oostra M, *et al.* (2007) Localization and membrane topology of coronavirus nonstructural
952 protein 4: involvement of the early secretory pathway in replication. *J Virol* 81(22):12323-
953 12336.
- 954 48. Knoops K, *et al.* (2010) Integrity of the early secretory pathway promotes, but is not required
955 for, severe acute respiratory syndrome coronavirus RNA synthesis and virus-induced
956 remodeling of endoplasmic reticulum membranes. *J Virol* 84(2):833-846.
- 957 49. Vogels MW, *et al.* (2011) Identification of host factors involved in coronavirus replication by
958 quantitative proteomics analysis. *Proteomics* 11(1):64-80.
- 959 50. Hsu NY, *et al.* (2010) Viral reorganization of the secretory pathway generates distinct
960 organelles for RNA replication. *Cell* 141(5):799-811.
- 961 51. Jackson RJ, Hellen CU, & Pestova TV (2010) The mechanism of eukaryotic translation initiation
962 and principles of its regulation. *Nat Rev Mol Cell Biol* 11(2):113-127.
- 963 52. Raaben M, *et al.* (2010) The ubiquitin-proteasome system plays an important role during
964 various stages of the coronavirus infection cycle. *J Virol* 84(15):7869-7879.
- 965 53. Lundin A, *et al.* (2014) Targeting membrane-bound viral RNA synthesis reveals potent
966 inhibition of diverse coronaviruses including the middle East respiratory syndrome virus. *PLoS*
967 *Pathog* 10(5):e1004166.
- 968 54. Bailey-Elkin BA, *et al.* (2014) Crystal structure of the Middle East respiratory syndrome
969 coronavirus (MERS-CoV) papain-like protease bound to ubiquitin facilitates targeted
970 disruption of deubiquitinating activity to demonstrate its role in innate immune suppression. *J*
971 *Biol Chem* 289(50):34667-34682.
- 972 55. David A, *et al.* (2012) Nuclear translation visualized by ribosome-bound nascent chain
973 puromycylation. *J Cell Biol* 197(1):45-57.
- 974 56. Randall G, *et al.* (2007) Cellular cofactors affecting hepatitis C virus infection and replication.
975 *Proc Natl Acad Sci U S A* 104(31):12884-12889.
- 976 57. Reid DW, *et al.* (2018) Dengue Virus Selectively Annexes Endoplasmic Reticulum-Associated
977 Translation Machinery as a Strategy for Co-opting Host Cell Protein Synthesis. *J Virol* 92(7).
- 978 58. Desmet EA, Anguish LJ, & Parker JS (2014) Virus-mediated compartmentalization of the host
979 translational machinery. *MBio* 5(5):e01463-01414.
- 980 59. Hashem Y, *et al.* (2013) Hepatitis-C-virus-like internal ribosome entry sites displace eIF3 to
981 gain access to the 40S subunit. *Nature* 503(7477):539-543.
- 982 60. Lee AS, Burdeinick-Kerr R, & Whelan SP (2013) A ribosome-specialized translation initiation
983 pathway is required for cap-dependent translation of vesicular stomatitis virus mRNAs. *Proc*
984 *Natl Acad Sci U S A* 110(1):324-329.
- 985 61. Lundin A, *et al.* (2014) Targeting Membrane-bound Viral RNA Synthesis Reveals Potent
986 Inhibition of Diverse Coronaviruses Including the Middle East Respiratory Syndrome Virus.
987 *PLoS Pathog*.
- 988 62. Thiel V, Herold J, Schelle B, & Siddell SG (2001) Infectious RNA transcribed in vitro from a
989 cDNA copy of the human coronavirus genome cloned in vaccinia virus. *J Gen Virol* 82(Pt
990 6):1273-1281.
- 991 63. van Boheemen S, *et al.* (2012) Genomic characterization of a newly discovered coronavirus
992 associated with acute respiratory distress syndrome in humans. *MBio* 3(6).
- 993 64. Bermingham A, *et al.* (2012) Severe respiratory illness caused by a novel coronavirus, in a
994 patient transferred to the United Kingdom from the Middle East, September 2012. *Euro*
995 *Surveill* 17(40):20290.

- 996 65. Lam SS, *et al.* (2015) Directed evolution of APEX2 for electron microscopy and proximity
997 labeling. *Nat Methods* 12(1):51-54.
- 998 66. Roux KJ, Kim DI, & Burke B (2013) BioID: a screen for protein-protein interactions. *Curr Protoc*
999 *Protein Sci* 74:Unit 19 23.
- 1000 67. Gosert R, Kanjanahaluethai A, Egger D, Bienz K, & Baker SC (2002) RNA replication of mouse
1001 hepatitis virus takes place at double-membrane vesicles. *J Virol* 76(8):3697-3708.
- 1002 68. Gunasekera K, Wuthrich D, Braga-Lagache S, Heller M, & Ochsenreiter T (2012) Proteome
1003 remodelling during development from blood to insect-form *Trypanosoma brucei* quantified by
1004 SILAC and mass spectrometry. *BMC Genomics* 13:556.
- 1005 69. Braga-Lagache S, *et al.* (2016) Robust Label-free, Quantitative Profiling of Circulating Plasma
1006 Microparticle (MP) Associated Proteins. *Mol Cell Proteomics* 15(12):3640-3652.
- 1007 70. Huang da W, Sherman BT, & Lempicki RA (2009) Systematic and integrative analysis of large
1008 gene lists using DAVID bioinformatics resources. *Nat Protoc* 4(1):44-57.
- 1009 71. Huang da W, Sherman BT, & Lempicki RA (2009) Bioinformatics enrichment tools: paths
1010 toward the comprehensive functional analysis of large gene lists. *Nucleic Acids Res* 37(1):1-13.
- 1011 72. Ashburner M, *et al.* (2000) Gene ontology: tool for the unification of biology. The Gene
1012 Ontology Consortium. *Nat Genet* 25(1):25-29.
- 1013 73. The Gene Ontology C (2017) Expansion of the Gene Ontology knowledgebase and resources.
1014 *Nucleic Acids Res* 45(D1):D331-D338.
- 1015 74. Carbon S, *et al.* (2009) AmiGO: online access to ontology and annotation data. *Bioinformatics*
1016 25(2):288-289.
- 1017 75. Simillion C, Liechti R, Lischer HE, Ioannidis V, & Bruggmann R (2017) Avoiding the pitfalls of
1018 gene set enrichment analysis with SetRank. *BMC Bioinformatics* 18(1):151.
- 1019 76. Krummenacker M, Paley S, Mueller L, Yan T, & Karp PD (2005) Querying and computing with
1020 BioCyc databases. *Bioinformatics* 21(16):3454-3455.
- 1021 77. Zheng G, *et al.* (2008) ITFP: an integrated platform of mammalian transcription factors.
1022 *Bioinformatics* 24(20):2416-2417.
- 1023 78. Kanehisa M, *et al.* (2014) Data, information, knowledge and principle: back to metabolism in
1024 KEGG. *Nucleic Acids Res* 42(Database issue):D199-205.
- 1025 79. Hornbeck PV, *et al.* (2012) PhosphoSitePlus: a comprehensive resource for investigating the
1026 structure and function of experimentally determined post-translational modifications in man
1027 and mouse. *Nucleic Acids Res* 40(Database issue):D261-270.
- 1028 80. Croft D, *et al.* (2014) The Reactome pathway knowledgebase. *Nucleic Acids Res* 42(Database
1029 issue):D472-477.
- 1030 81. Kelder T, *et al.* (2012) WikiPathways: building research communities on biological pathways.
1031 *Nucleic Acids Res* 40(Database issue):D1301-1307.
- 1032 82. Szklarczyk D, *et al.* (2017) The STRING database in 2017: quality-controlled protein-protein
1033 association networks, made broadly accessible. *Nucleic Acids Res* 45(D1):D362-D368.
- 1034 83. Szklarczyk D, *et al.* (2015) STRING v10: protein-protein interaction networks, integrated over
1035 the tree of life. *Nucleic Acids Res* 43(Database issue):D447-452.
- 1036 84. Livak KJ & Schmittgen TD (2001) Analysis of relative gene expression data using real-time
1037 quantitative PCR and the 2(-Delta Delta C(T)) Method. *Methods* 25(4):402-408.
- 1038 85. Shen Z, *et al.* (2018) Structural Basis for the Inhibition of Host Gene Expression by Porcine
1039 Epidemic Diarrhea Virus nsp1. *J Virol* 92(5).
- 1040 86. Schatz G, *et al.* (2013) Ciliary beating plane and wave propagation in the bovine oviduct. *Cells*
1041 *Tissues Organs* 198(6):457-469.
- 1042
- 1043

1044 **Supplemental Figure 1.** Immunofluorescence analysis of MHV-BirA_{R118G}-nsp2-mediated
1045 biotinylation. MHV-BirA_{R118G}-nsp2, MHV-A59- or non-infected L929 fibroblasts were
1046 cultured in medium supplemented with 67 μ M biotin. Cells were fixed 12 hours post infection
1047 (h.p.i.) and processed for immunofluorescence analysis with antibodies directed against the
1048 BirA_{R118G} (anti-myc), the viral replicase (anti-nsp2/3 or nsp8) and biotinylated factors
1049 (streptavidin). Nuclei are counterstained with DAPI. Z-projection of deconvolved z-stacks
1050 acquired with a DeltaVision Elite High-Resolution imaging system are shown. Scale bars: 20
1051 μ m.

1052

1053 **Supplemental Figure 2.** STRING protein interaction network analysis of the categories “cell
1054 organization” (a) and “catabolic processes” (b). The nodes represent RTC-proximal host
1055 proteins and the edges represent the interactions, either direct (physical) or indirect
1056 (functional), between two proteins in the network.

1057

1058 **Supplemental Figure 3.** (a) siRNA controls contained in each 96-well plate during siRNA-
1059 silencing of the RTC-proximal library. Controls included the established factors such as MHV
1060 entry receptor (Ceacam1a), Gbfl1, Arf1. Arfgap2 was found to moderately affect MHV
1061 replication during pilot experiments and was included to cover the entire inhibitory range. (b)
1062 Cell viability following 48h siRNA-silencing of components of the cellular translation
1063 machinery. (c) Expression levels of Rpl13a, eIF3E, eIF3I, eIF3F, eIF4G1, eIF4G2, eIF2ak3,
1064 Rsl24d1 following siRNA knockdown compared to expression levels in cells treated with non-
1065 targetting siRNA. (d) Visual inspection of L929 treated with siRNA targetting eIF3E, eIF3I,
1066 eIF3F, Rrbp1, Rpl13a, non-targetting siRNA (scramble). Note that RNA silencing (b) and
1067 translation activity (c) in Rpl13a-silenced cells could not be assessed, likely due to cytotoxicity

1068 observed by visual inspection of cells. (e) Western blot and western blot analysis of total
1069 cellular translation. Upon 48h siRNA-silencing, L929 fibroblasts were pulsed with 3 μ M
1070 puromycin for 60 min. Control cells were treated, prior to puromycin incubation, with 355 μ M
1071 cycloheximide and 208 μ M Emetin for 30 min to block protein synthesis. Western blots were
1072 probed using anti-puromycin antibodies to assess puromycin incorporation into polypeptides
1073 and normalized to actin levels. Error bars represent the mean \pm standard deviation of three
1074 independent experiments, where * is ** is $p \leq 0.005$.

1075

1076 **Supplemental Figure 4.** Visualization of active translation during HCoV-229E infections.
1077 Huh7 cells were infected with HCoV-229E (MOI=1) for 12, 15, 18, 24 h. Cells were pulsed
1078 with cycloheximide, emetine and puromycin for 5min to label translating ribosomes and
1079 subjected to a coextraction/fixation procedure to remove free puromycin. Non-infected and/or
1080 non-pulsed cells were used as control. Cells were labelled using anti-nsp8 (HCoV-229E) and
1081 anti-puromycin antibodies. Nuclei are counterstained with DAPI. Z-projection of deconvolved
1082 z-stacks acquired with a DeltaVision Elite High-Resolution imaging system are shown.
1083 Intensity profiles of magnified regions are shown. Scale bar: 20 μ m.

Figure 1

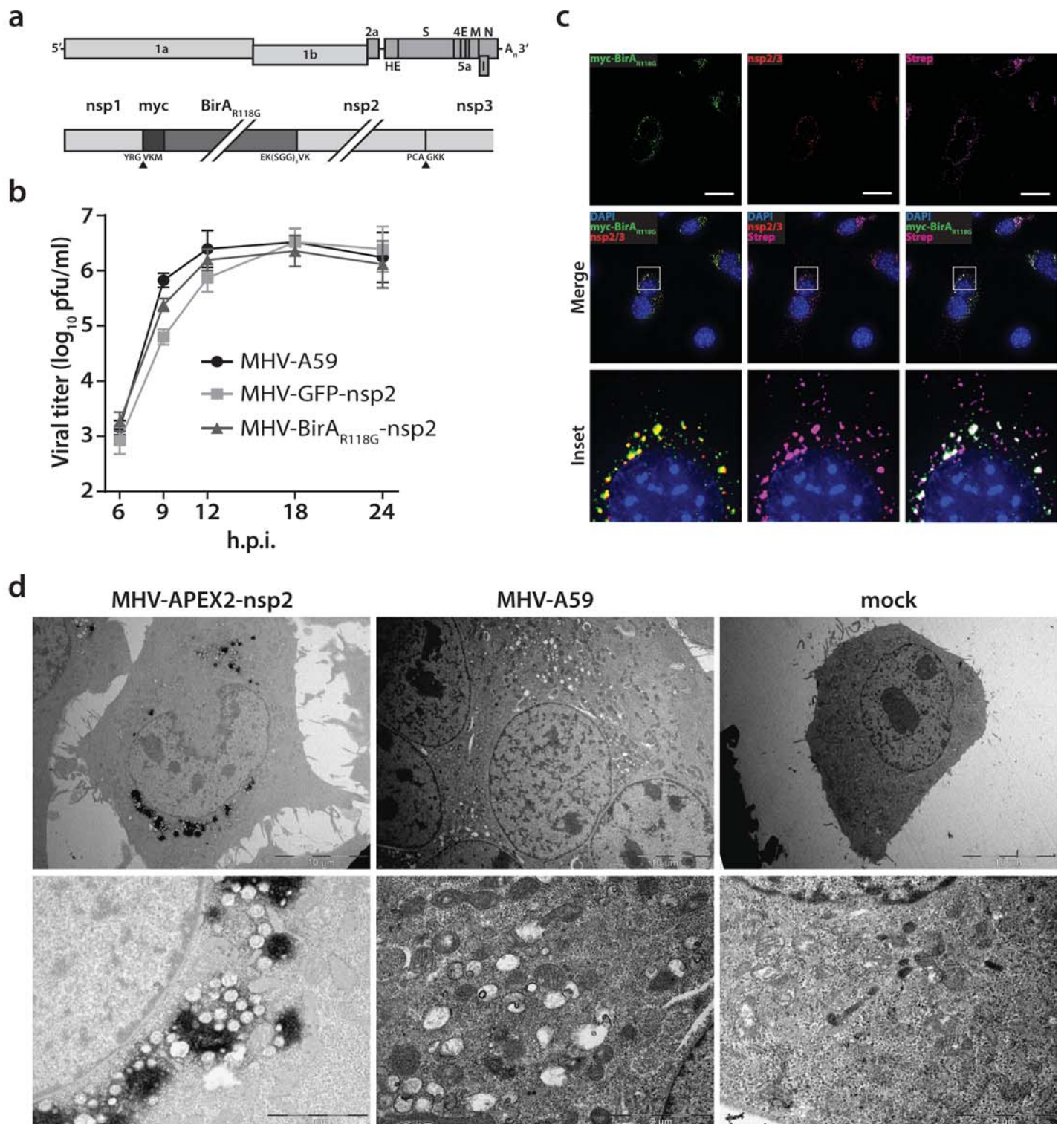


Figure 2

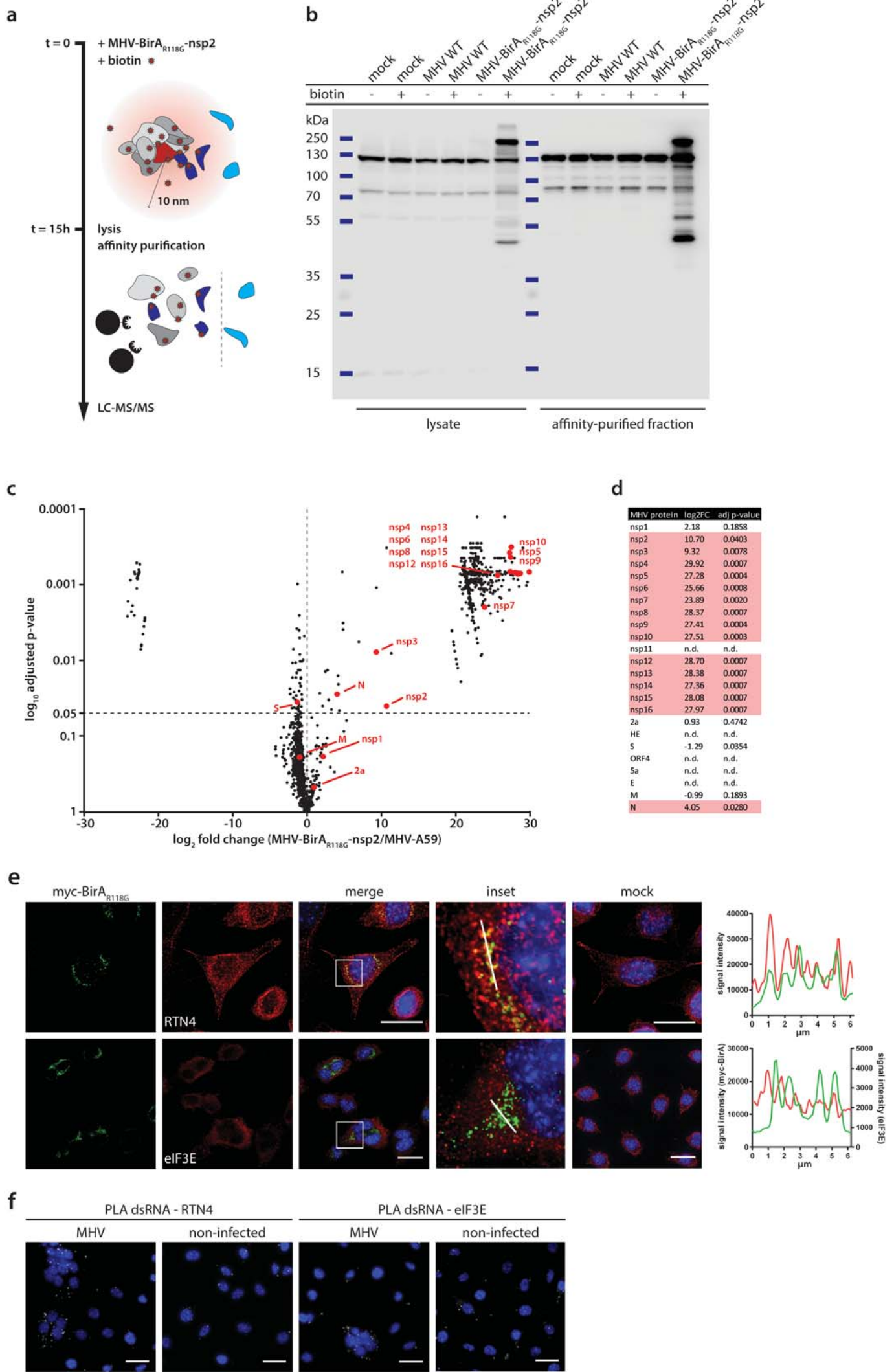


Figure 3

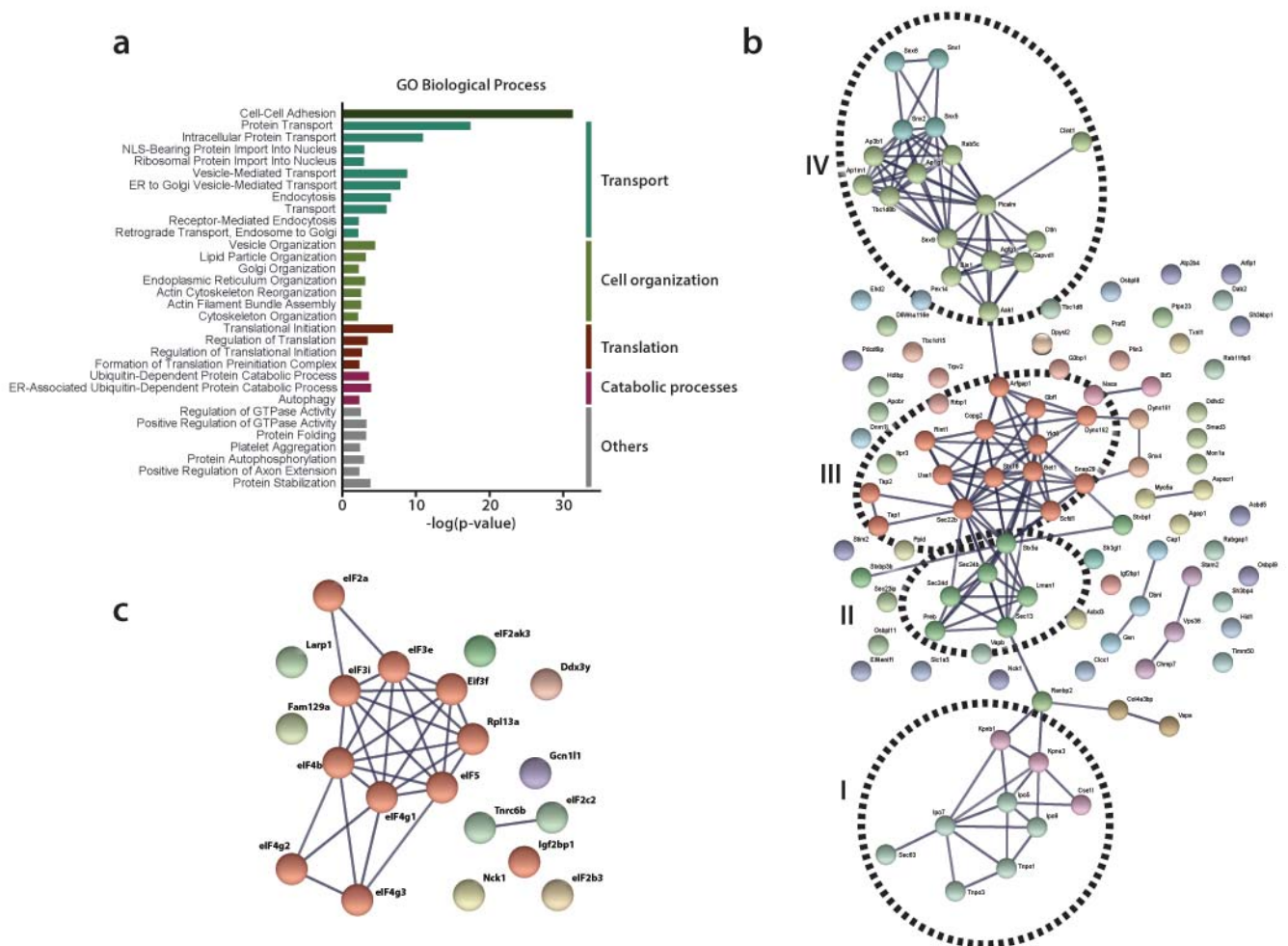


Figure 4

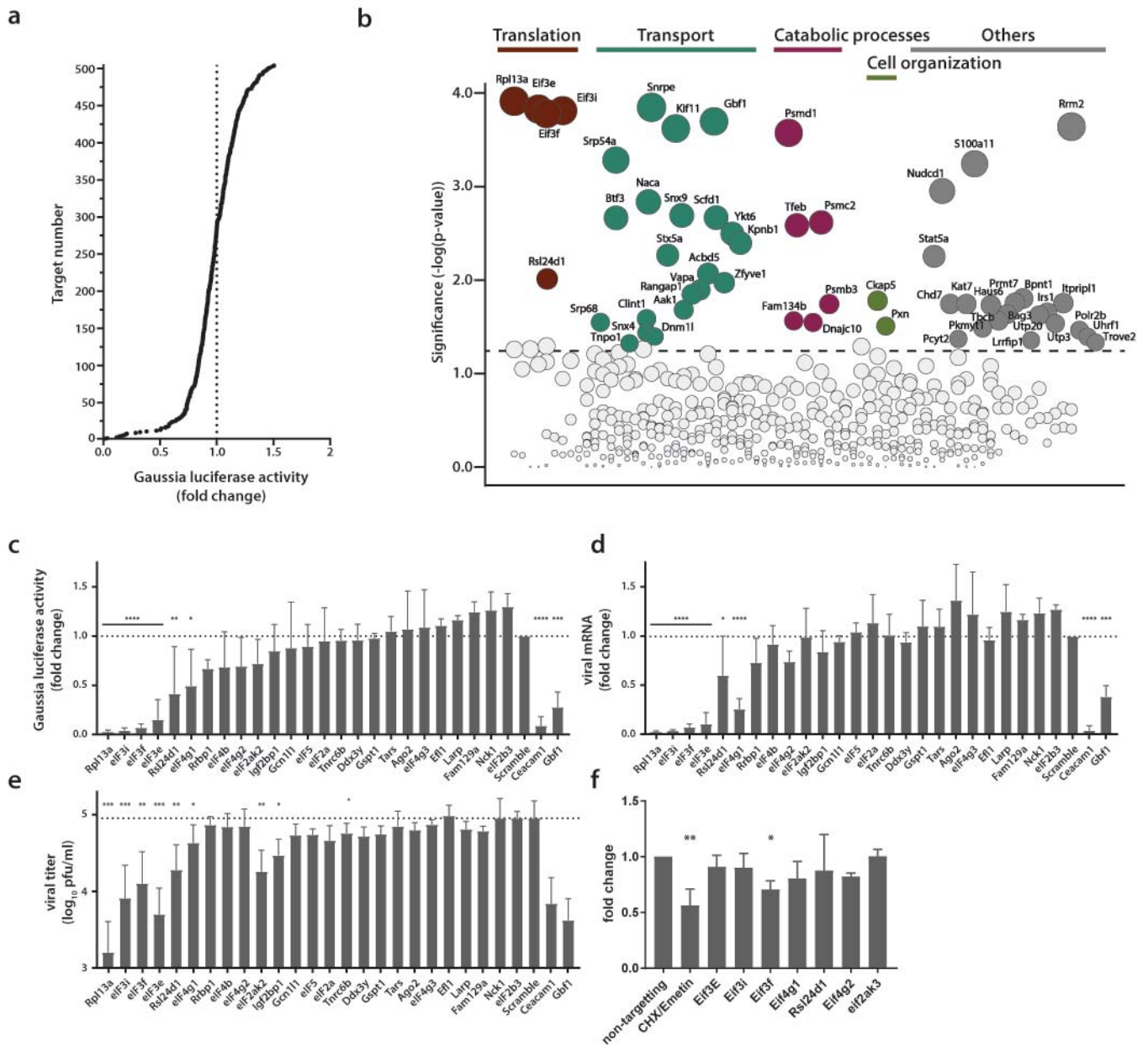


Figure 5

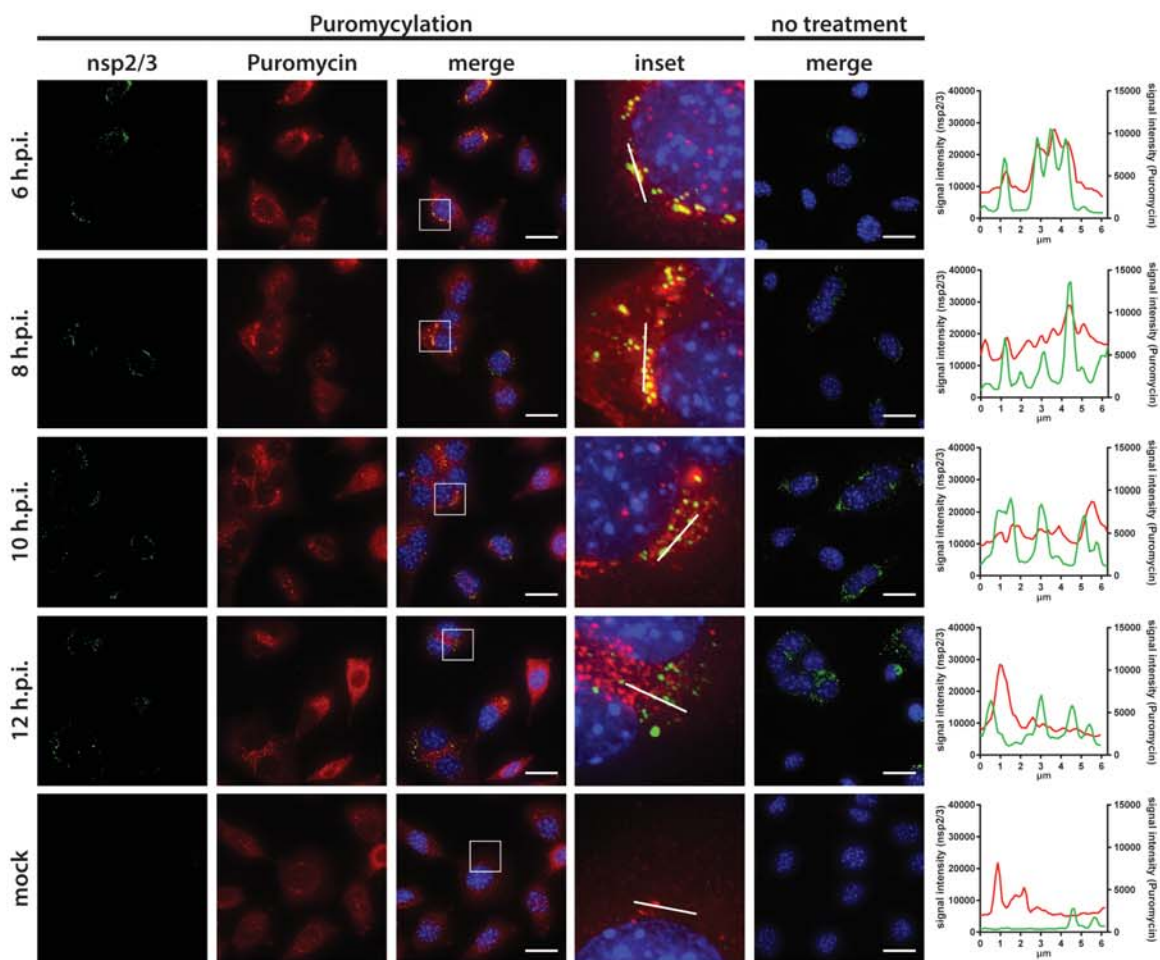
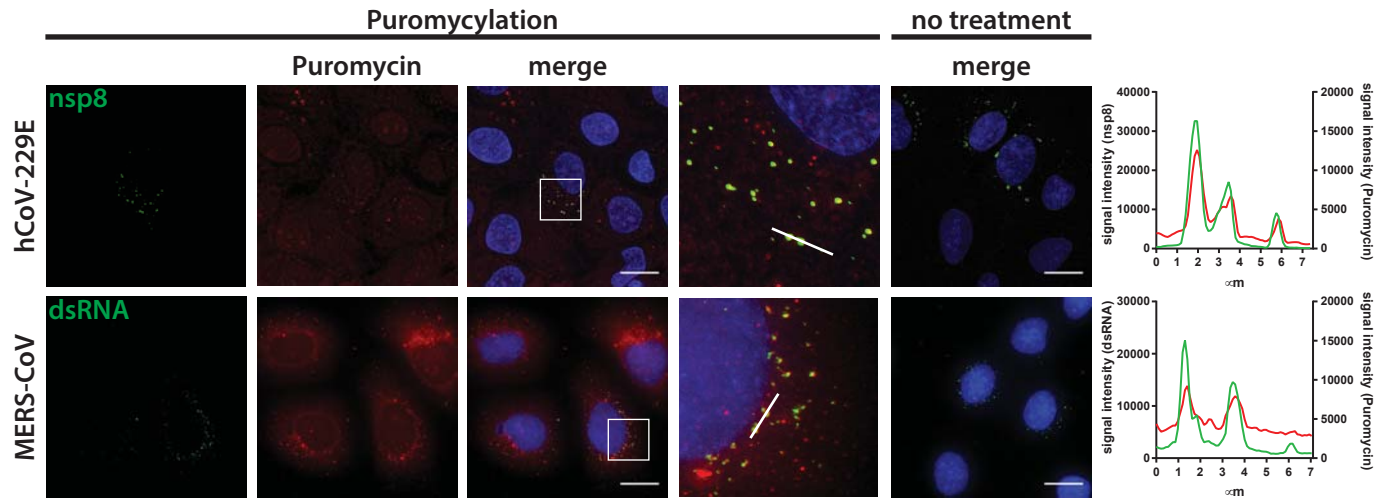


Figure 6



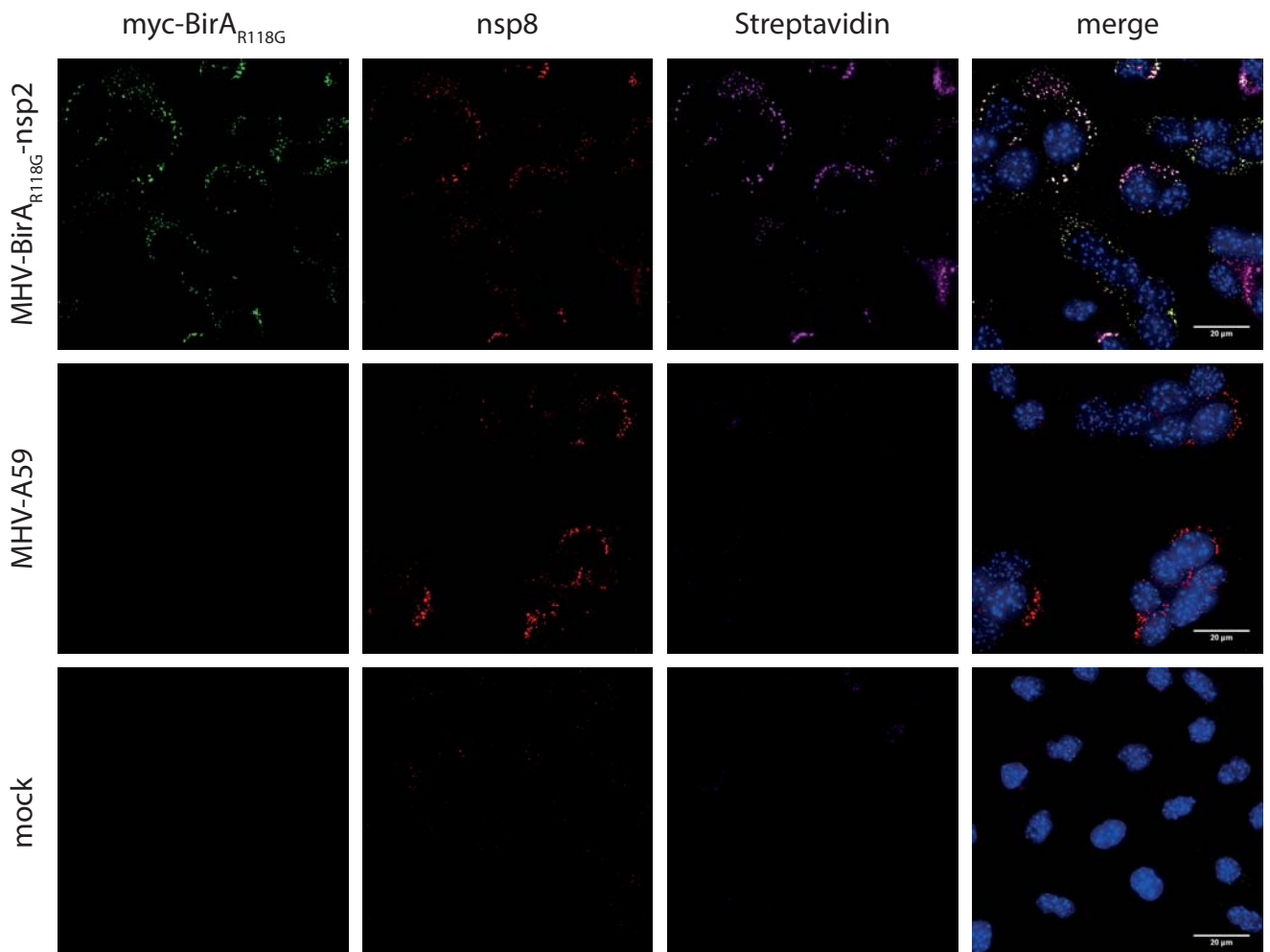
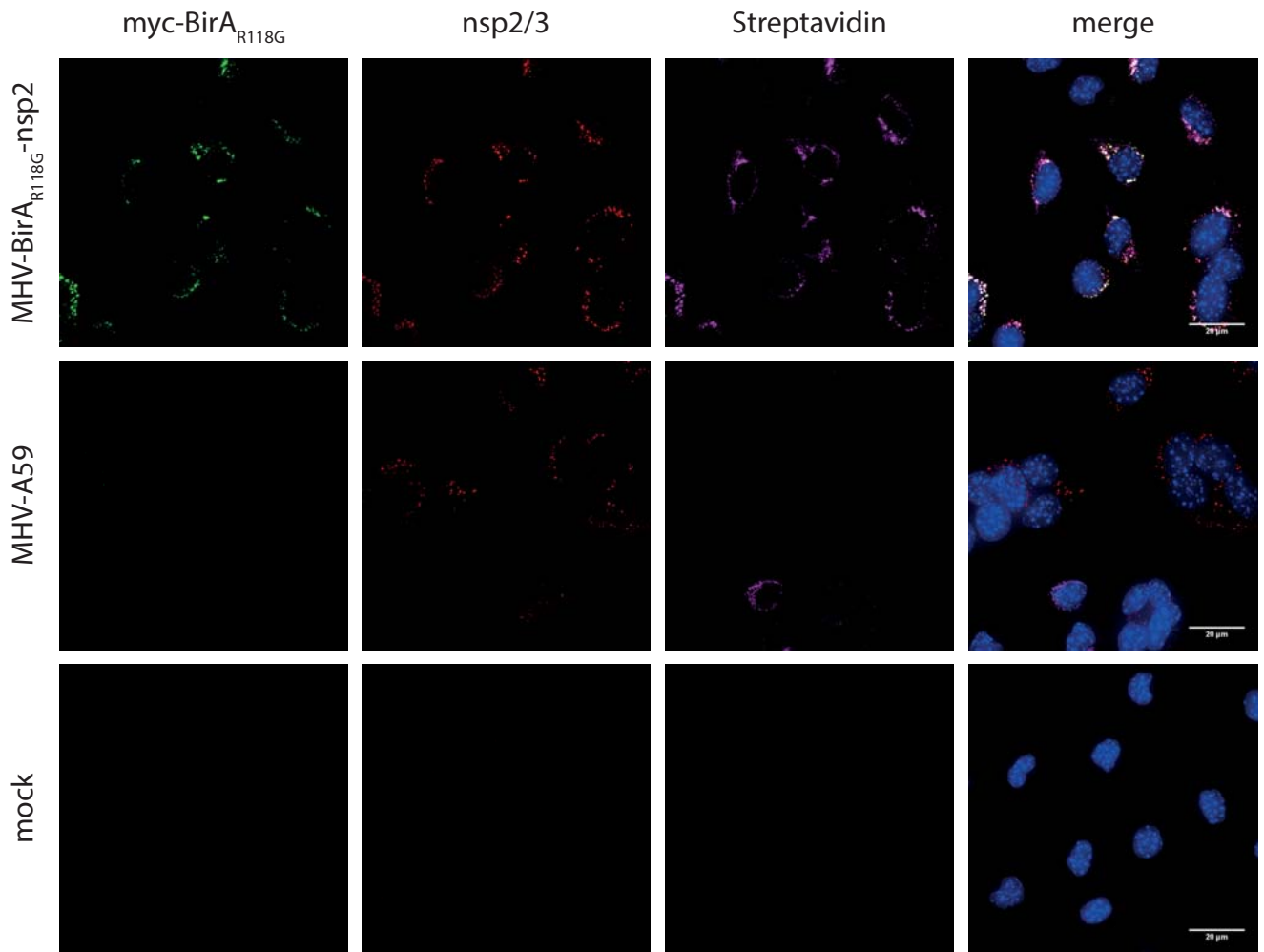
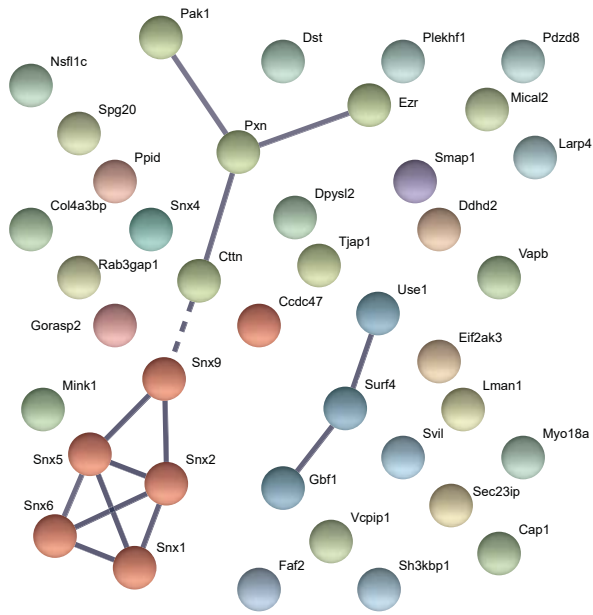


Figure S2

a



b

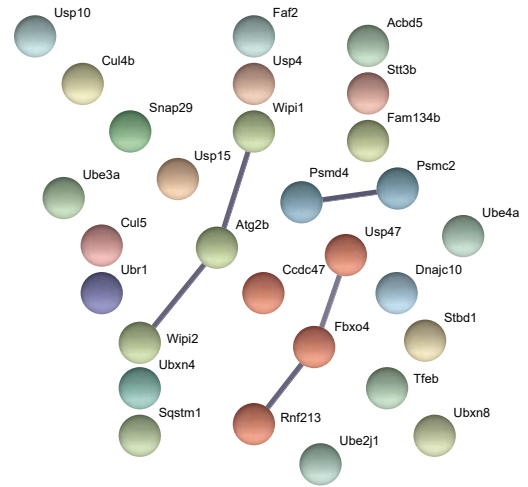


Figure S3

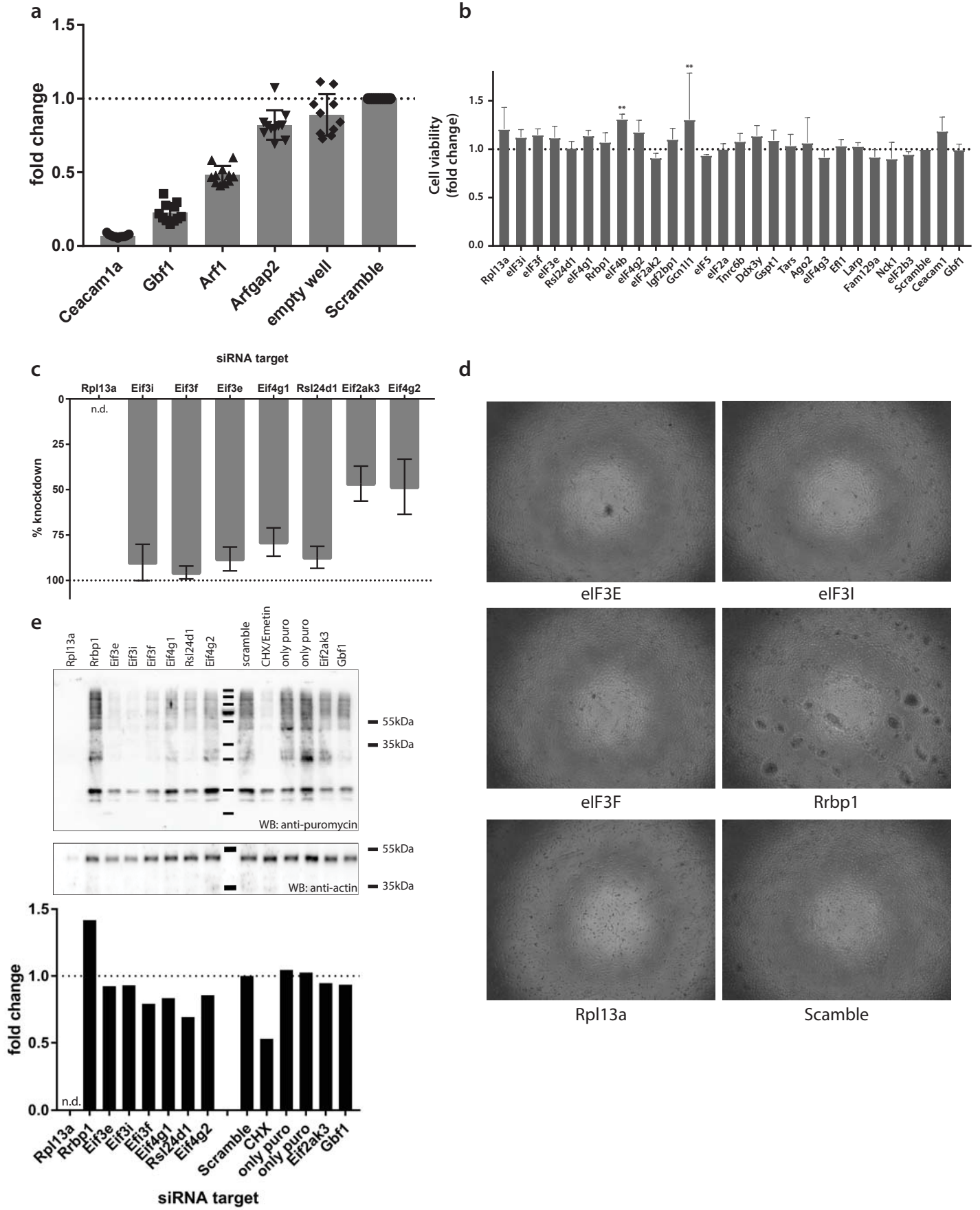


Figure S4

